

The diverse meteorology of Jezero crater over the first 250 sols of Perseverance on Mars

Received: 8 May 2022

Accepted: 21 October 2022

Published online: 9 January 2023

 Check for updates

A list of authors and their affiliations appears at the end of the paper

NASA's Perseverance rover's Mars Environmental Dynamics Analyzer is collecting data at Jezero crater, characterizing the physical processes in the lowest layer of the Martian atmosphere. Here we present measurements from the instrument's first 250 sols of operation, revealing a spatially and temporally variable meteorology at Jezero. We find that temperature measurements at four heights capture the response of the atmospheric surface layer to multiple phenomena. We observe the transition from a stable night-time thermal inversion to a daytime, highly turbulent convective regime, with large vertical thermal gradients. Measurement of multiple daily optical depths suggests aerosol concentrations are higher in the morning than in the afternoon. Measured wind patterns are driven mainly by local topography, with a small contribution from regional winds. Daily and seasonal variability of relative humidity shows a complex hydrologic cycle. These observations suggest that changes in some local surface properties, such as surface albedo and thermal inertia, play an influential role. On a larger scale, surface pressure measurements show typical signatures of gravity waves and baroclinic eddies in a part of the seasonal cycle previously characterized as low wave activity. These observations, both combined and simultaneous, unveil the diversity of processes driving change on today's Martian surface at Jezero crater.

The Perseverance rover landed on 18 February 2021 at 18.44° N 77.45° E, near the northwest rim of Jezero crater, on the inner northwest slopes of Isidis Planitia¹. On board the rover is the most complete environmental station sent to date to another planet: the Mars Environmental Dynamics Analyzer (MEDA) instrument². It includes new capabilities, compared with previous missions^{3–8}, that enable better characterization of the diversity of physical processes driving near-surface environmental changes in Jezero. MEDA acquires data autonomously, on a regular and configurable basis, in sessions that typically cover more than 50% of a sol. Sampling sessions, typically one hour long, alternate every sol between even and odd hours, allowing for a complete characterization of daily and seasonal cycles every other sol (Extended Data Fig. 1 shows the temporal coverage of the measurements made). MEDA also

provides context for the investigations that other rover instruments and systems are conducting and supports the planning of Ingenuity flights, as well as landing of a possible future mission to return samples collected by Perseverance.

In this Article, we present results for the first 250 sols of the mission (solar longitudes $L_s = 6^\circ$ – 121°), northern hemisphere spring to early summer.

The active atmospheric surface layer

The atmospheric surface layer (ASL) is the lower part of the atmosphere in direct interaction with the surface, having a depth that varies on Mars from a few metres during daytime to tens of metres at night^{9,10}. In the ASL, energy and mass exchanges between surface and atmosphere

✉ e-mail: manfredi@cab.inta-csic.es; manuel.delatorrejuarez@jpl.nasa.gov; agustin.sanchez@ehu.eus

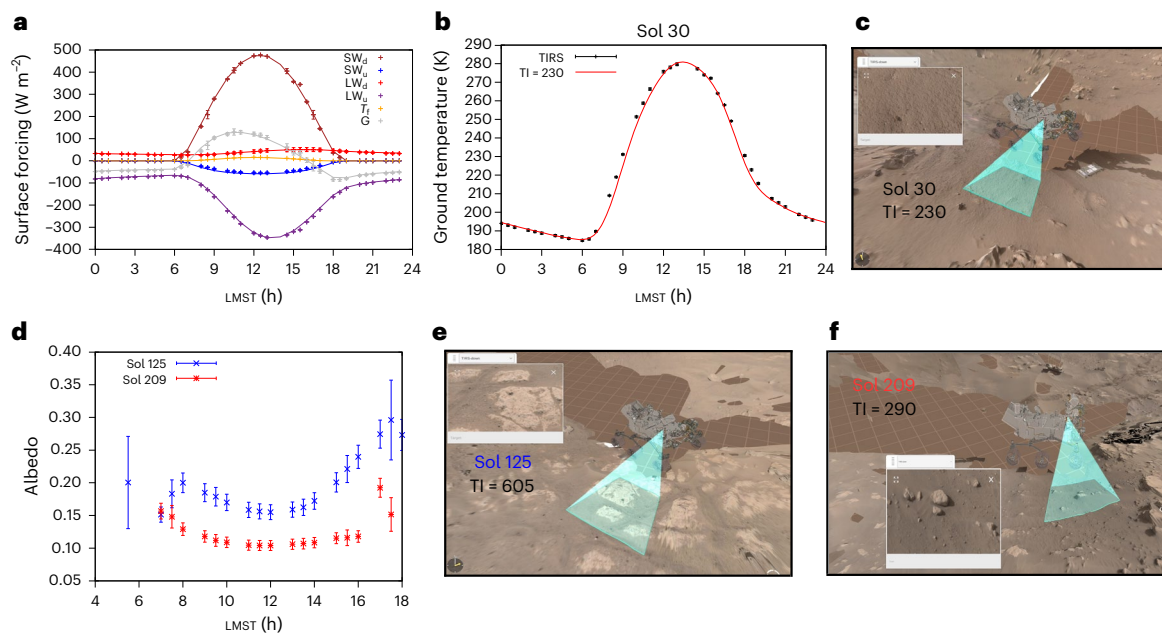


Fig. 1 | SEB components measured in situ in Jezero. **a**, Diurnal variation of the SEB on sol 30 obtained from MEDA (symbols) and simulated with single-column models (solid lines; for further details, see Methods and Extended Data Fig. 2). **b**, Ground temperature measured by MEDA (black symbols) and obtained by solving the heat conduction equation (solid red line) using MEDA's net heat flux, G . The best fit is obtained for $TI = 230 \text{ J m}^{-2} \text{ K}^{-1} \text{ s}^{-1/2}$. **c**, Footprint (green shade) of the ground temperature sensor on sol 30. For horizontal terrains, this footprint covers an area of a few square metres. **d**, Diurnal evolution of broadband albedo on sols 125 (blue) and 209 (red). The albedo shows a minimum close to noon,

with increasing values as the solar zenith angle increases. This non-Lambertian behaviour is similar in other sols, regardless of the type of terrain and geometry of the rover. **e, f**, As in **c**, for sols 125 (**e**) and 209 (**f**), with MEDA-derived TI values of 605 and 290 $\text{J m}^{-2} \text{ K}^{-1} \text{ s}^{-1/2}$, respectively. Shown data result from the mean of 300 samples at the beginning and half of each hour, plus or minus the standard deviation. LMST, Local Mean Solar Time; SW_d , downwelling solar flux; SW_u , solar flux reflected by the surface; LW_d , downwelling long-wave atmospheric flux; LW_u , upwelling long-wave flux emitted by the surface; T_p , turbulent heat flux. Credit: panels **c, e, f** from NASA/JPL-Caltech.

occur, and its hydrological cycle provides constraints on the photochemistry of surface and near-surface air. Most of the atmospheric dynamics in this layer are driven by radiative processes¹⁰. Albedo, net radiative flux and thermal inertia are key elements of that forcing and result in the radiative surface energy budget (SEB). MEDA's thermal infrared sensor (TIRS) and radiation and dust sensor (RDS) enable quantification of all SEB terms (see Methods for a detailed description of each term) on the surface of Mars (Fig. 1a), an important step in improving the predictive capabilities of numerical models.

When Perseverance is parked every sol, TI is obtained by minimizing the difference between measured and numerically simulated values of the diurnal amplitude of ground temperature (Fig. 1b). The MEDA-derived TI values range from 180 to 605 $\text{J m}^{-2} \text{ K}^{-1} \text{ s}^{-1/2}$, as in Gale, ref. 11. The surface albedo (Fig. 1d) is obtained around the clock, using downwelling (0.2–1.2 μm) and reflected (0.3–3.0 μm) solar flux measurements (Fig. 1c, e, f). A radiative transfer model, COMIMART¹², is used to convert both fluxes to 0.2–5.0 μm . The SEB is then measured and used as an upper boundary condition to solve the heat conduction equation for homogeneous terrains in models^{13,14}. Figure 1a, b shows the diurnal cycle of retrieved fluxes and surface temperature, respectively.

Figure 1d shows the diurnal evolution of measured albedo on the sols with the highest (sol 125) and lowest (sol 209) values of the studied period. On both sols, the minimum value is reached near noon and increases as solar zenith angle (SZA) approaches 90°. The relative maximum at -8:00 and -17:00 occurs when $SZA = -55^\circ$ and the specular reflection is within TIRS field of view (FoV). This behaviour points to non-Lambertian albedo at the surface, not observable from surface satellites in nadir pointing.

Importantly, modelling of the thermal and radiative environment shows that the effect of the radioisotope thermoelectric generator (RTG) on TIRS FoV ground heating is negligible. This fact has been

verified by careful analysis of the ground temperature in consideration of the winds, which indicate that the effects are $<0.5 \text{ K}$.

Near-surface thermal profile

Another new feature enabled by MEDA is the simultaneous tracking of temperatures at four heights—surface, 0.85 m, 1.45 m and about 40 m—around the clock (Fig. 2a). The variation of these temperatures along a sol reflects the four main regimes of the ASL: (1) daytime convection, (2) an evening transition where the convective boundary layer collapses, (3) a night-time steady regime and (4) a morning transition where the inversion fades and a convective boundary layer grows. Figure 2b–d shows an example of the daily evolution of the thermal gradient. Daytime convection peaks at noon with the maximum of the derivative of the temperature (T , in Kelvin) with the height (z , in meters) $(dT/dz)_{\text{max}} \approx -35 \text{ K m}^{-1}$ while night-time stable stratification peaks at 20:00 with $(dT/dz)_{\text{max}} \approx +8 \text{ K m}^{-1}$ in the first metre from the surface, reaching values well above the adiabatic gradient $g/C_p = 0.0045 \text{ K m}^{-1}$. Figure 2e shows the seasonal evolution of mean temperatures, where the daily average thermal gradient is dominated by the daytime convective period. In most sols, night-time thermal stability weakens as the night progresses, and unstable conditions often develop from 2:00 onward.

A similar observation was reported for InSight¹⁵ and attributed to the radiative influence of the hardware. In addition, Curiosity's Rover Environmental Monitoring Station instrument, measuring on the deeper Gale crater, has seen this inversion broken only during the global dust storm¹⁶. With MEDA, we observe that the night-time inversion depends on the local terrain properties. Measurements over high TI terrain result in the break-up of the night-time thermal inversion due to warm night-time surfaces (Extended Data Fig. 3). However, air temperatures at different levels are not sensitive to the TI of the specific terrain, and the influence of the terrain on air temperatures

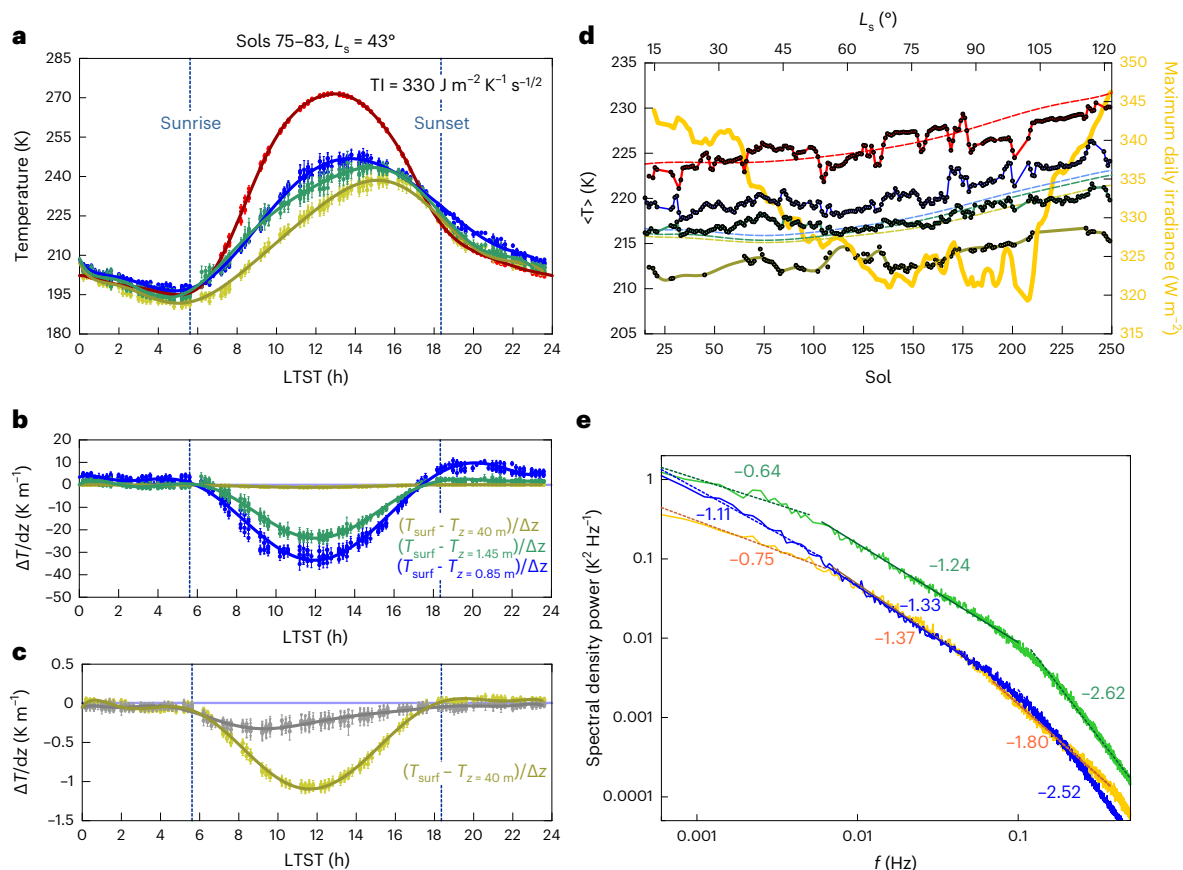


Fig. 2 | Daily cycle of temperatures under typical values of TI. **a**, Temperature at the surface (T_{surf} ; red), at $z = 0.85$ m (blue), $z = 1.45$ m (green) and $z = 40$ m (green yellow). **b**, Thermal gradients from the surface to the near surface at 0.85 m (blue) and 1.45 m (green). **c**, Thermal gradient from the surface to 40 m (green yellow) and from 1.45 m to 40 m (grey). The adiabatic thermal gradient, $dT/dz = -0.0047$ K m^{-1} , is shown in **b** and **c** with a horizontal light-blue line (a horizontal line that is partially covered by the curve $(T_{\text{surf}} - T_z = 40 \text{ m})/\Delta z$, which can be seen quite well in the center of the figure (LTST from 10 to 15 h)). Shown data in **a–c** result from the mean on 12 min intervals (740 samples), plus or minus

the standard deviation. **d**, Seasonal evolution of mean daily air temperatures. TIRS and atmospheric temperature sensor temperatures (solid lines) at the surface (red), $z = 0.85$ m (blue), $z = 1.45$ m (green) and $z = 40$ m (green yellow) are compared with predictions from the Mars Climate Database²¹ (dashed lines). Yellow line shows the maximum irradiance measured by RDS. **e**, Statistical analysis of power spectra of temperature fluctuations at 0.85 m (blue), 1.45 m (green) and 40 m (yellow) between $10:00$ and $15:00$ h. Lines show the fit to the data in each frequency range. Figures reflect the estimated exponential indices. $TI = 330$ $\text{J m}^{-2} \text{K}^{-1} \text{s}^{-1/2}$. Dots are averages over a 12 min window. LTST, local true solar time.

decreases progressively from 0.85 to 40.00 m (Fig. 2d and Extended Data Fig. 3). Winds driven by horizontal gradients of surface thermal properties¹⁷ may be the origin of the discrepancies we observe from measurements with respect to the predictions from one-dimensional radiative equilibrium models.

Temperature fluctuations are common throughout the sol; these rise after sunrise, peaking near noon (amplitudes $\Delta T_{\text{max}} \approx 10$ K), and are convective in nature. These subside before sunset and increase again during the break-up of the night-time inversion, suggesting strong nocturnal fluctuations (Extended Data Fig. 4). The oscillations are created by turbulent processes in the atmosphere whose characteristics can be investigated by analysing the spectral power density of temperatures, pressures and winds^{18–20}. Figure 2e shows the power spectral densities of temperatures during the convective period, averaged over 250 sols. The results show typical slopes of turbulence in daytime hours, with changes at other times of the sol; these will be analysed in later works. MEDA enables the identification of different dynamical regimes, forced, inertial and dissipative, more clearly than with previous instruments^{19,20} and at different altitudes.

Pressure fluctuations

Turbulence is also present in pressure and horizontal wind measurements. Figure 3a shows examples of the daily pressure cycle on different

sols; this cycle has the contribution of different dynamic phenomena, as discussed in the following. Analysis of the rapid pressure fluctuations shows a power spectrum similar to that of temperature (Extended Data Fig. 5), different from that expected from Kolmogorov turbulence but similar to that measured by InSight¹⁵. During the stable night-time period, the pressure fluctuations are at the detector noise level.

Convection generates transient events detectable through several MEDA sensors, especially in temperature and pressure data (Extended Data Fig. 6). Some events are dust devils (DDs), also detected as slight drops (~ 0.4 – 26.0%) in radiation sensor readings or imaged with Perseverance cameras²². Jezero exhibits the highest abundance of DDs so far detected by a mission on the surface of Mars^{23,24}. The pressure drops detected in this period range from ~ 0.3 to 6.5 Pa in intensity and last from 1 to 200 s. DDs where simultaneous MEDA wind data are available have estimated diameters from 5 to 135 m (ref. 23), with vortices having rotational speeds of -4 – 24 m s^{-1} . A small number of these produced measurable albedo changes on the surface as they removed dust, observed through variations in the upward/downward radiation ratio measured with TIRS and RDS sensors (Extended Data Fig. 7)²³.

Wind speeds show a daily cycle, with maximum values of 7 m s^{-1} in the afternoon and near null between $4:00$ and $6:00$ (Fig. 3b). Strong gusts are detected with maximum speeds of 25 m s^{-1} at midday. Turbulence creates fluctuating winds of about 2 – 4 m s^{-1} at night, where they

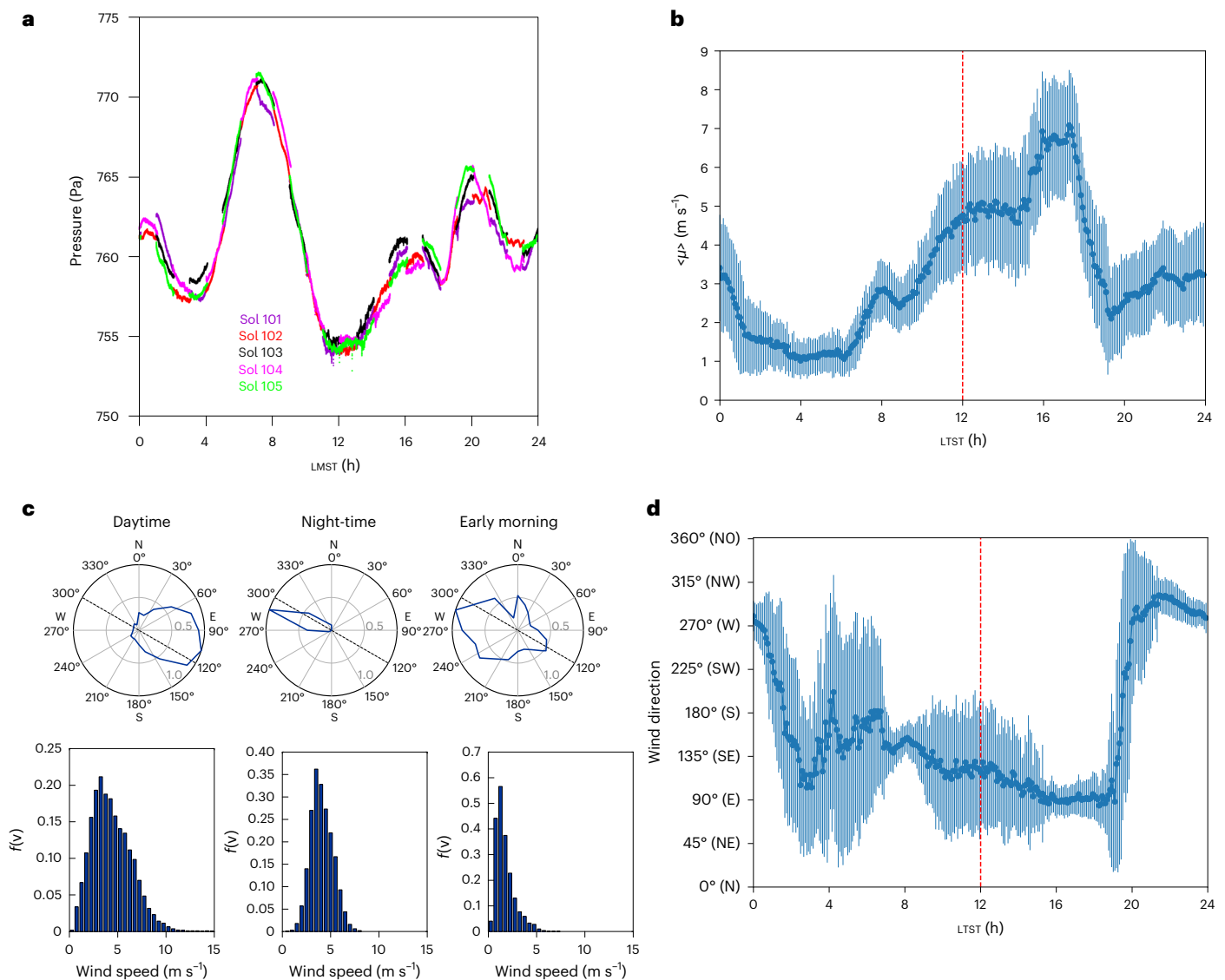


Fig. 3 | Fluctuations in the daily pressure cycle and wind patterns. **a**, Daily pressure cycles for sols 101–105, showing deviations from the mean values (in 10 s intervals) caused by different dynamic phenomena. **b**, Mean values of wind intensity, averaged in intervals of 5 min. Error bars show the standard deviations. **c**, Wind azimuths in different time slots (dotted lines, -120° azimuth, show the regional slope direction in the Isidis basin). We observe that upward winds

predominate during the day and downward winds during the night, a trend attributable to local flows acting in Jezero and the interaction with other scales (top). Histogram of wind speed at those hours, that is, the frequency distribution of the occurrence of each speed, $f(v)$ (bottom). **d**, Mean directions from which the winds blow, averaged in intervals of 5 min. Error bars show the standard deviations.

are probably responses to horizontal shear flows²⁵, and $5\text{--}7\text{ m s}^{-1}$ during the convective hours (Fig. 3c). Pre-landing atmospheric modelling predicted that daytime upflows and night-time downflows on the Isidis basin slopes would dominate the overall wind pattern, with Jezero local topography causing a relatively small but measurable effect^{13,14}. Wind data support the dominance of daytime upslope currents from roughly southeast, with a reversal of winds at night¹⁴ (Fig. 3c,d). These diurnal wind patterns drive aeolian erosion at Jezero²³ and show a variety of behaviours resulting from a complex interaction among regional circulation, slope winds and interaction with the general circulation and the large-scale Hadley cell flow.

Atmospheric dust properties

SkyCam is tracking the regular morning–evening opacity cycle in the $600\text{--}800\text{ nm}$ wavelength range as a function of time (Fig. 4a)². During the clear season covered by this study, persistently higher opacity is observed in the morning (optical depth (OD) ~ 0.5) than in the afternoon

(OD ~ 0.4) (refs. 26,27). Analysis of RDS data at different wavelengths and observation geometries allows determination of the optical properties of the dust, and derivation of the OD variation at high temporal resolution, similar to the more sparsely sampled Viking record²⁸ (Fig. 4b). The dust optical properties and OD are estimated by comparing the temporal variation of the measured sky spectral intensity with radiative transfer simulations (Fig. 4c shows an example). Most of the particle-size information is obtained when the Sun trajectory is near one of the RDS lateral sensor's FoV. From these observations, we found particle sizes ranging from ~ 1.2 to $1.4\ \mu\text{m}$, consistent with previous studies^{29–31}, with corrections suggested by refs. 32–34. To estimate the non-sphericity of those particles, the T-matrix approach was used to compute the phase function, single-scattering albedo and extension cross section.

These first sols of the mission fell within the aphelion cloud belt season and near the peak latitude for water-ice clouds³⁵. It is therefore likely that some of the afternoon opacity in Fig. 4a, including the

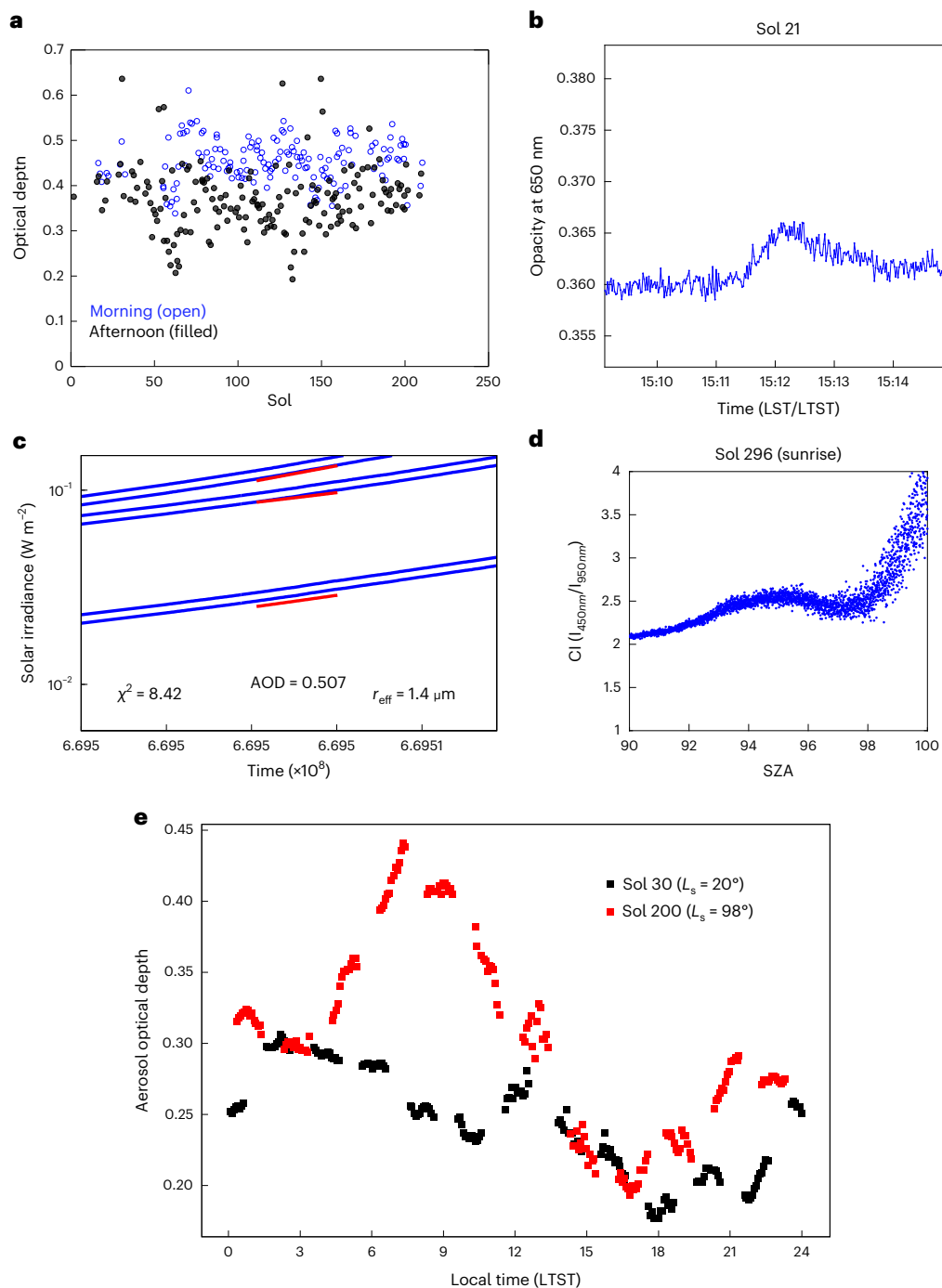


Fig. 4 | Daily monitoring of atmospheric opacity and characterization of dust particles and clouds. **a**, OD derived from SkyCam images to follow the day–night cycle in the visual range (550 nm). Values are observed to be higher in the morning than in the afternoon, consistent with measurements made occasionally with MastCam-Z²². **b**, RDS observations also allow the derivation of the OD at a temporal resolution of 1 s, enabling the study of short-duration events, such as DD. An example of a temporal increase in opacity due to a nearby DD occurred on sol 21 around 15:11. **c**, An example of dust particle radius and OD

estimation using RDS observations at different wavelengths and radiative transfer simulations. The best fit is obtained for an effective radius $r_{\text{eff}} = 1.4 \mu\text{m}$. **d**, Variation of the colour index (CI), defined as the ratio between RDS observations at zeniths at 450 and 950 nm (ref. 41) to the SZA measured on sol 296. The SZA of maximum CI indicates that this cloud layer is above 45 km. **e**, Aerosol OD (AOD) at 9 μm retrieved from TIRS observations for sols 30 and 200. TIRS observations enable AOD to be retrieved at all local times. The large diurnal variation for sol 200 is probably caused by water-ice clouds.

increase around sol 70 and most of the morning–afternoon difference, is due to water-ice hazes^{36,37}. Clouds were observed around sols 70 and 180, but discrete clouds were not typically present during daytime²². During this season, a low dust OD (0.3–0.6), with low variability, is typical of other sites^{38,39}. We have also found cloud signatures during daytime and twilight. In the latter cases (Fig. 4d)⁴⁰, we could constrain

the cloud altitudes using radiative transfer simulations⁴¹. In most cases, we found cloud altitudes around or above 40 km and particle sizes larger than 1 μm (indicative of water-ice particles).

The daily OD evolution was also retrieved from TIRS infrared measurements, strengthening the case for night-time clouds. Figure 4e shows the diurnal variation of thermal infrared aerosol OD, contributed

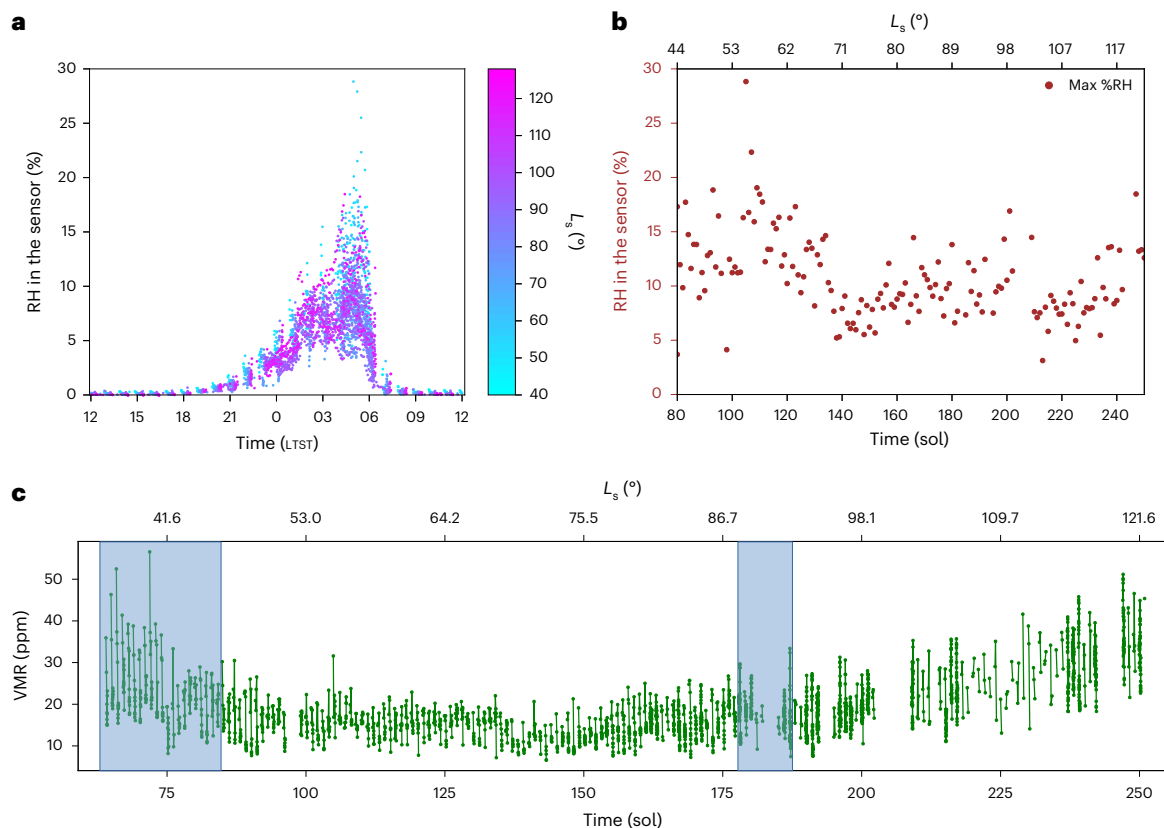


Fig. 5 | Daily and seasonal cycles of RH and VMR observed at Jezero. **a**, Daily and seasonal evolution of RH for sols 80–250, L_s 44–122°. The uncertainty in the estimation of this magnitude, which is temperature dependent, is <3.5% in the temperature range recorded by HS. **b**, Seasonal evolution of the maximum RH values observed, reaching an absolute maximum of 29% RH, referring to the temperature recorded by HS itself, for sols 80–250, L_s 44–122°. **c**, Seasonal

behaviour of the night-time VRM derived from RH for sols 64–250, averaging seconds 2–5 from the beginning of each acquisition session. The uncertainty in the estimation of this magnitude, for the temperatures and the RH range shown in **a**, is <20%. Maintenance regeneration heatings of the sensor heads are marked as blue bars (these data should not be taken into consideration).

by both dust and water-ice clouds, as a function of local time for two representative sols. Because TIRS observes thermal infrared radiation, this retrieval is possible for all local times, including during the night, a capability not available on previous rovers except by Mini-TES on board Mars Exploration Rover, which could make only limited and occasional night-time observations⁴². The OD observed by TIRS during sol 30 ($L_s = 20^\circ$) shows a moderate variation with greater opacity at night than during the day. By sol 200, the aphelion season cloud belt⁴³ was near its peak annual amplitude, and data reveal a notable diurnal variation in OD with maximum clouds shortly after dawn. This ability to track OD throughout each sol is a powerful tool that leads to new insights about how dust and water-ice clouds interact with the surface and the rest of the atmosphere.

A complex humidity cycle

Measuring the relative humidity (RH) in the ASL on diurnal and seasonal timescales is a key element in understanding hydrological processes in the Martian atmosphere⁴⁴. MEDA's humidity sensor (HS) often finds a nocturnal hydrological cycle more complex than anticipated in numerical predictions¹³. Figure 5a shows the daily and seasonal behaviour of RH, while Fig. 5b shows the daily maxima recorded in the period studied. Likewise, Fig. 5c shows the seasonal variations of night-time water-vapour volume mixing ratio (VMR). Within the diurnal cycle, the maximum, typically in the range 15–30% in RH (referring to HS temperature), occurs in the early morning, with maximum VMR being reached around midnight. Nocturnal water-vapour amounts at Jezero during the seasons are lower than those at Gale and model predictions¹³.

MEDA measured a seasonal minimum in night-time VMR near $L_s = 70^\circ$, with higher abundance and greater variability at the end of the season (Fig. 5c). In addition, a large increase in VMR was observed on the evening of sol 104 (see Extended Data Fig. 8 for details of the evolution of VMR and RH on those sols), accompanied by cooling atmospheric temperatures. The increase in RH slowly returned to typical values, while the temperature continued dropping. This behaviour may be due to a single dry air mass advected over the rover bringing cold, dry air, which then remains in the area. An alternative explanation is that it is related to the local surface and possible exchange processes. In the early morning of sol 105, frost conditions were possible as seen by comparing the calculated frost point (at 1.45 m) with the TIRS ground temperature. A resulting hypothesis is that, if subsurface exchange is occurring, the actual frost point at the atmosphere–surface interface may be lower owing to less vapour present in the atmosphere.

Non-local dynamical phenomena

The daily pressure cycles at Jezero showed a rich variability, reflecting the action of different dynamical mechanisms in the atmosphere under a variety of spatial and temporal scales (Fig. 3a). On the seasonal scale, as the northern polar cap sublimated, the daily mean pressure increased from 735 Pa on sols 15–20 ($L_s = 13^\circ$ – 16°) to a maximum of 761 Pa on sols 99–110 ($L_s = 52^\circ$ – 57°). It then gradually decreased to 650 Pa in sol 250 ($L_s = 125^\circ$) as the southern polar cap grew (Fig. 6a).

Extended Data Fig. 9a shows the deviations of the daily pressure averages of Fig. 6a from a polynomial fit of degree 5, observing oscillations with periods in the range of 3–5 sols and amplitudes varying between 1 and 3 Pa, a signature of what could be high-frequency

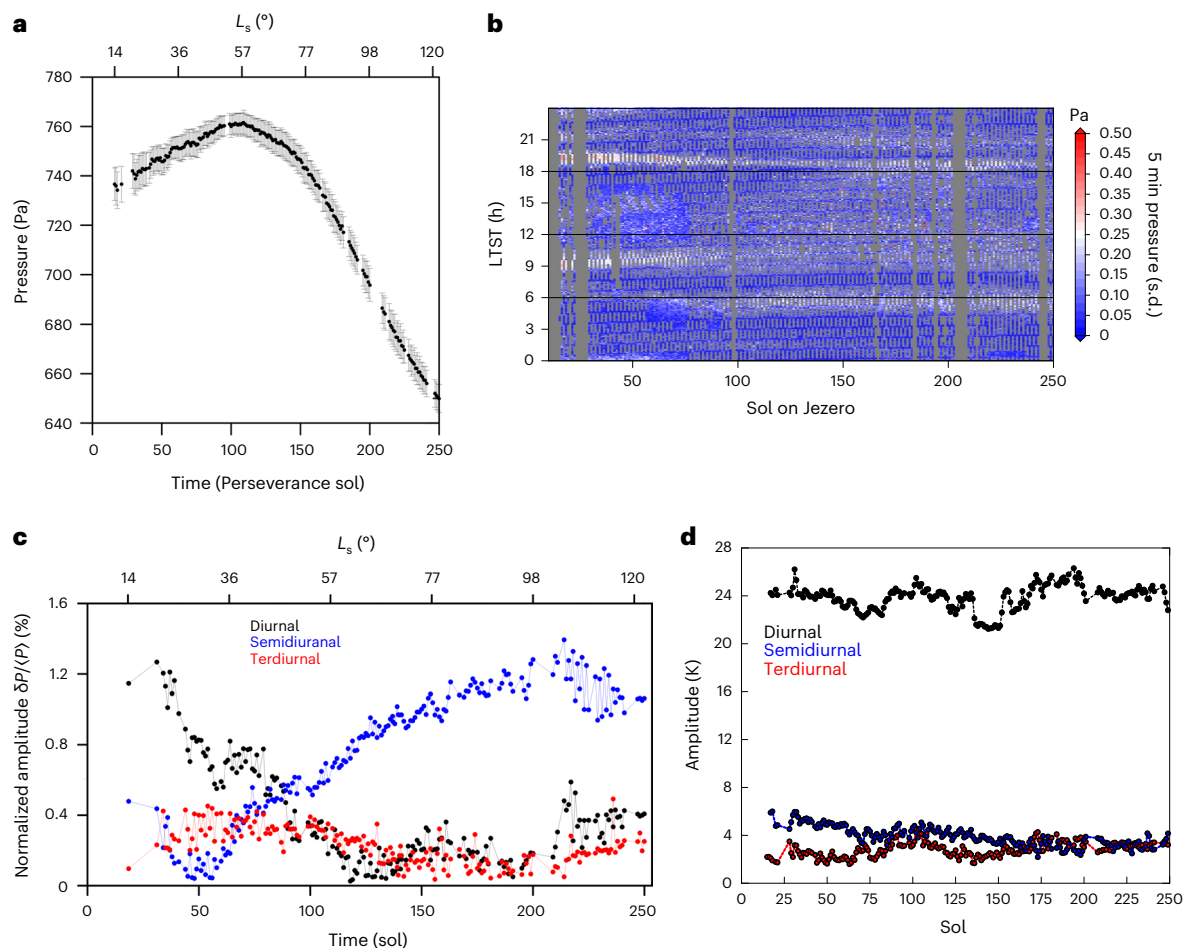


Fig. 6 | Atmospheric pressure variability as a consequence of various dynamic mechanisms at various scales. a, Seasonal evolution of daily mean pressure values and their daily ranges. **b**, Detrended standard deviation of pressure, as a function of sol and LTST, after subtracting least squares fit of the observed pressure. Removing the tidal components shows that the dominant contribution

to pressure variability occurs during the hours with strong convection and after a calm period. **c**, The first three components of the Fourier analysis of the pressure cycle: diurnal (24 h period; black), semidiurnal (12 h period; blue) and terdiurnal (6 h period; red) components. **d**, Equivalent Fourier analysis of the temperature data at $z = 1.45$ m: diurnal (blue) and semidiurnal (red) components.

travelling waves arising from baroclinic instabilities also reported elsewhere¹³. In addition, Extended Data Fig. 9b shows the regular oscillations of the residuals resulting from a fit to the approximately 1 h measurement series that, on average, have a peak-to-peak amplitude of 0.2–0.4 Pa and periods between 12 and 20 min. The properties of these oscillations are similar to those reported in Gale, observed by the Rover Environmental Monitoring Station instrument on the Curiosity rover⁴⁵ and in Elysium Planitia by the InSight mission¹⁵, which have been interpreted as produced by the passage of gravity waves. Figure 6b shows the seasonal and diurnal pressure variability where the daily patterns of pressure changes are observed.

Thermal tides cause the large modulation of the daily pressure (P) cycle⁴⁶. A Fourier analysis of that cycle shows that up to six components are present, with maximum amplitudes ranging from 0.2 to 10.0 Pa. Figure 6c shows the wide variability of the normalized amplitude of diurnal and semidiurnal tides. The maximum relative change observed in the studied period is $(\delta P/P)_{\max} \approx 0.013$. Smaller changes also occurred in tidal components 3 and 4. The semidiurnal component showed a very strong drop between sols 20 and 50; although still under investigation, it may suggest a relation to the dust loading present on those sols or the development of disturbances at the polar cap edge⁴⁶. Tides are also detected in the Fourier analysis of the temperature data with half amplitudes of 26 K (diurnal), 2–6 K (semidiurnal) and 2–4 K (terdiurnal), as shown in Fig. 6d. The tidal variability is related mainly to

changes in atmospheric opacity produced by clouds and dust loading at different altitudes²². The period studied is the non-dusty season on Mars, which makes the variability relatively low.

A rich and dynamic near-surface environment

Mars 2020 mission includes a payload to monitor an environment that exhibits a rich diversity of behaviours. Many of the measurements made by MEDA so far are the first time they have been obtained on Mars, revealing interesting surprises in Jezero's atmosphere.

The SEB is measured for the first time in situ. The design of future engineering systems, the understanding and modelling of photochemical reactions at the surface and the interpretation of satellite measurements benefit from these results. An example is the characterization of the non-Lambertian reflection of the surface that must be considered in the interpretation of orbital observations of variations in albedo when trying to understand changes in the physical properties of the surface.

Globally, the measured daily temperature cycle agrees with model predictions (although with some deviations in the vertical temperature gradient), expected magnitude of thermal oscillations and the seasonal evolution. In addition, the observed vortex convective activity matches the predictions of large eddy simulation using the MarsWRF model²³. However, when analysing vertical temperature profiles, we find a diversity of nocturnal responses that raise intriguing questions about what is happening at the different locations traversed by the rover.

Several independent radiation sensors and methods have measured the occurrence and even development of night-time clouds long before the peak of the cloud season. The ability to track OD throughout each sol is a powerful tool that has shown the prevalence of clouds near dawn and will lead to new insights about how dust and water-ice clouds interact with the surface and the rest of the atmosphere.

The observed nocturnal hydrologic cycle is more complex than anticipated by the models and is also observed in Gale. This unpredicted behaviour can be due to a variety of causes yet to be explored in detail.

Thermal tides show smaller pressure amplitudes at Jezero when compared with Curiosity's observations⁴⁷ or Viking⁴⁸. While the general behaviour at Jezero was predicted by the models^{13,14}, there are differences in its amplitude and timing probably due to the interaction of local topography with the air mass exchanges between the interior and exterior of the basin. Another interesting result is the existence of multisol waves at a time of the season when baroclinic waves have been observed to have very limited activity⁴⁶.

Overall, MEDA observations show a dynamic environment rich in atmospheric phenomena that is different from other locations on Mars studied by previous missions. The characterization of Jezero's atmosphere plays an important role in the development of the Mars Sample Return mission and in the exposure of the samples being collected by Perseverance.

Online content

Any methods, additional references, Nature Portfolio reporting summaries, source data, extended data, supplementary information, acknowledgements, peer review information; details of author contributions and competing interests; and statements of data and code availability are available at <https://doi.org/10.1038/s41561-022-01084-0>.

References

- Farley, K. A. et al. Mars 2020 mission overview. *Space Sci. Rev.* **216**, 142 (2020).
- Rodríguez-Manfredi, J. A. et al. The Mars Environmental Dynamics Analyzer, MEDA. A suite of environmental sensors for the Mars 2020 mission. *Space Sci. Rev.* **217**, 48 (2021).
- Hess, S. L., Henry, R. M., Leovy, C. B., Ryan, J. A. & Tillman, J. E. Meteorological results from the surface of Mars: Viking 1 and 2. *J. Geophys. Res.* **82**, 4559–4574 (1997).
- Schofield, J. T. et al. The Mars Pathfinder atmospheric structure investigation/meteorology (ASI/MET) experiment. *Science* **278**, 1752–1758 (1997).
- Taylor, P. A. et al. Temperature, pressure and wind instrumentation on the Phoenix meteorological package. *J. Geophys. Res.* **113**, EA0A10 (2008).
- Smith, M. D. et al. First atmospheric science results from the Mars Exploration Rovers Mini-TES. *Science* **306**, 1750–1753 (2004).
- Gómez-Elvira, J. et al. REMS: the environmental sensor suite for the Mars Science Laboratory rover. *Space Sci. Rev.* **170**, 583–640 (2012).
- Banfield, D. et al. InSight Auxiliary Payload Sensor Suite (APSS). *Space Sci. Rev.* **215**, 4 (2019).
- Petrosyan, A. et al. The Martian atmospheric boundary layer. *Rev. Geophys.* **49**, 2010RG000351 (2011).
- Read, P. L., Lewis, S. R. & Mulholland, D. P. The physics of Martian weather and climate: a review. *Rep. Prog. Phys.* **78**, 125901 (2015).
- Martínez, G. M. et al. The surface energy budget at Gale crater during the first 2500 sols of the Mars Science Laboratory mission. *J. Geophys. Res. Planets* **126**, e2020JE006804 (2021).
- Vicente-Retortillo, Á., Valero, F., Vázquez, L. & Martínez, G. M. A model to calculate solar radiation fluxes on the Martian surface. *J. Space Weather Space Clim.* **5**, A33 (2015).
- Pla-García, J. et al. Meteorological predictions for Mars 2020 Perseverance rover landing site at Jezero Crater. *Space Sci. Rev.* **216**, 148 (2020).
- Newman, C. et al. Multi-model meteorological and aeolian predictions for Mars 2020 and the Jezero Crater region. *Space Sci. Rev.* **217**, 20 (2021).
- Banfield, D. et al. The atmosphere of Mars as observed by InSight. *Nat. Geo.* **13**, 190–198 (2020).
- Guzewich, S. D. et al. Mars Science Laboratory observations of the 2018/Mars year 34 global dust storm. *Geophys. Res. Lett.* <https://doi.org/10.1029/2018GL080839> (2019).
- Siili, T. Modeling of albedo and thermal inertia induced mesoscale circulations in the midlatitude summertime Martian atmosphere. *J. Geophys. Res. Planets* **101**, 14957–14968 (1996).
- Tillman, J. E., Landberg, L. & Larsen, S. E. The boundary layer of Mars: fluxes, stability, turbulent spectra, and growth of the mixed layer. *J. Atmos. Sci.* **51**, 1709–1727 (1994).
- Larsen, S. E., Jørgensen, H. E., Landberg, L. & Tillman, J. E. Aspects of the atmospheric surface layers on Mars and Earth. *Boundary Layer Meteorol.* **105**, 451–470 (2002).
- Davy, R. et al. Initial analysis of air temperature and related data from the Phoenix MET station and their use in estimating turbulent heat fluxes. *J. Geophys. Res.* **115**, E00E13 (2010).
- Millour, E. et al. The Mars climate database (MCD version 5.2). *EPSC Abstr.* **10**, abstr. 438 (2015).
- Bell, J. F. III et al. Geological, multispectral, and meteorological imaging results from the Mars 2020 Perseverance rover in Jezero crater. *Sci. Adv.* **8**, eabo4856 (2022).
- Newman, C. E. et al. The dynamic atmospheric and aeolian environment of Jezero Crater, Mars. *Sci. Adv.* **8**, eabn3782 (2022).
- Ellehoj, M. D. et al. Convective vortices and dust devils at the Phoenix Mars mission landing site. *J. Geophys. Res.* **115**, E00E16 (2010).
- Read, P. L. et al. in *The Atmosphere and Climate of Mars* (eds Haberle, R. M. et al.) Ch. 7 (Cambridge Univ. Press, 2017); <https://doi.org/10.1017/9781139060172.007>
- Kahre, M. et al. in *The Atmosphere and Climate of Mars* (eds Haberle, R. M. et al.) Ch. 10 (Cambridge Univ. Press, 2017); <https://doi.org/10.1017/9781139060172.010>
- Tamppari, L. K., Zurek, R. W. & Paige, D. A. Viking-era diurnal water-ice clouds. *J. Geophys. Res.* **108**, 5073 (2003).
- Colburn, D. S., Pollack, J. B. & Haberle, R. M. Diurnal variations in optical depth at Mars. *Icarus* **79**, 159–189 (1989).
- Stamnes, K., Tsay, S. C., Wiscombe, W. & Jayaweera, K. Numerically stable algorithm for discrete-ordinate-method radiative transfer in multiple scattering and emitting layered media. *Appl. Opt.* **27**, 2502–2509 (1988).
- Tomasko, M. G., Doose, L. R., Lemmon, M., Smith, P. H. & Wegryn, E. Properties of dust in the Martian atmosphere from the Imager on Mars Pathfinder. *J. Geophys. Res.* **104**, 8987–9007 (1999).
- Lemmon, M. T. et al. Atmospheric imaging results from the Mars Exploration rovers: spirit and opportunity. *Science* **306**, 1753–1756 (2004).
- Wolff, M. J. et al. Wavelength dependence of dust aerosol single scattering albedo as observed by the compact reconnaissance imaging spectrometer. *J. Geophys. Res.* **114**, E00D04 (2009).
- Lemmon, M. T. et al. Large dust aerosol sizes seen during the 2018 Martian global dust event by the Curiosity rover. *Geophys. Res. Lett.* **46**, 9448–9456 (2019).
- Chen-Chen, H., Pérez-Hoyos, S. & Sánchez-Lavega, A. Dust particle size and optical depth on Mars retrieved by the MSL navigation cameras. *Icarus* **319**, 43–57 (2019).
- Wolff, J. M. et al. Mapping water ice clouds on Mars with MRO/MARCI. *Icarus* **332**, 24–49 (2019).

36. Tamppari, L. K., Zurek, R. W. & Paige, D. A. Viking era water-ice clouds. *J. Geophys. Res.* <https://doi.org/10.1029/1999JE001133> (2000).
37. Hale, A. S., Tamppari, L. K., Bass, D. S. & Smith, M. D. Martian water ice clouds: a view from Mars Global Surveyor Thermal Emission Spectrometer. *J. Geophys. Res.* **116**, E04004 (2011).
38. Lemmon, M. T. et al. Dust aerosol, clouds, and the atmospheric optical depth record over 5 Mars years of the Mars Exploration Rover mission. *Icarus* **251**, 96–111 (2015).
39. Montabone, L. et al. Martian year 34 column dust climatology from Mars climate sounder observations: reconstructed maps and model simulations. *J. Geophys. Res. Planets* <https://doi.org/10.1029/2019JE006111> (2020).
40. Toledo, D. et al. Measurement of dust optical depth using the solar irradiance sensor (SIS) onboard the ExoMars 2016 EDM. *Planet. Space Sci.* **138**, 33–43 (2017).
41. Toledo, D., Rannou, P., Pommereau, J. P., Sarkissian, A. & Foujols, T. Measurement of aerosol optical depth and sub-visual cloud detection using the optical depth sensor (ODS). *Atmos. Meas. Tech.* **9**, 455–467 (2016).
42. Smith, M. D. et al. One Martian year of atmospheric observations using MER Mini-TES. *J. Geophys. Res.* **111**, E12S13 (2006).
43. Clancy, R. T. et al. in *The Atmosphere and Climate of Mars* (eds Haberle, R. M. et al.) Ch 5 (Cambridge Univ. Press, 2017); <https://doi.org/10.1017/9781139060172.005>
44. Tamppari, L. K. & Lemmon, M. T. Near-surface atmospheric water vapor enhancement at the Mars Phoenix lander site. *Icarus* <https://doi.org/10.1016/j.icarus.2020.113624> (2020).
45. Guzewich, S. D. et al. Gravity wave observations by the Mars Science Laboratory REMS pressure sensor and comparison with mesoscale atmospheric modeling with MarsWRF. *J. Geophys. Res. Planets* <https://doi.org/10.1029/2021je006907> (2021).
46. Barnes, J. R. et al. in *The Atmosphere and Climate of Mars* (eds Haberle, R. M. et al.) Ch. 9 (Cambridge Univ. Press, 2017); <https://doi.org/10.1017/9781139060172.009>
47. Haberle et al. Preliminary interpretation of the REMS pressure data from the first 100 sols of the MSL mission. *J. Geophys. Res. Planets* **119**, 440–453 (2014).
48. Zurek, R. W. Inferences of dust opacities for the 1977 Martian great dust storms from Viking Lander 1 pressure data. *Icarus* **45**, 202–215 (1981).

Publisher's note Springer Nature remains neutral with regard to jurisdictional claims in published maps and institutional affiliations.

Open Access This article is licensed under a Creative Commons Attribution 4.0 International License, which permits use, sharing, adaptation, distribution and reproduction in any medium or format, as long as you give appropriate credit to the original author(s) and the source, provide a link to the Creative Commons license, and indicate if changes were made. The images or other third party material in this article are included in the article's Creative Commons license, unless indicated otherwise in a credit line to the material. If material is not included in the article's Creative Commons license and your intended use is not permitted by statutory regulation or exceeds the permitted use, you will need to obtain permission directly from the copyright holder. To view a copy of this license, visit <http://creativecommons.org/licenses/by/4.0/>.

© The Author(s) 2023

J. A. Rodriguez-Manfredi¹✉, **M. de la Torre Juarez**²✉, **A. Sanchez-Lavega**³✉, **R. Hueso**³, **G. Martinez**⁴, **M. T. Lemmon**⁵, **C. E. Newman**⁶, **A. Manguira**³, **M. Hieta**⁷, **L. K. Tamppari**², **J. Polkko**⁷, **D. Toledo**⁸, **E. Sebastian**¹, **M. D. Smith**⁹, **I. Jaakonaho**⁷, **M. Genzer**⁷, **A. De Vicente-Retortillo**¹, **D. Viudez-Moreiras**¹, **M. Ramos**¹⁰, **A. Saiz-Lopez**¹¹, **A. Lepinette**¹, **M. Wolff**⁵, **R. J. Sullivan**¹², **J. Gomez-Elvira**¹, **V. Apestigue**⁸, **P. G. Conrad**¹³, **T. Del Rio-Gaztelurrutia**³, **N. Murdoch**¹⁴, **I. Arruego**⁸, **D. Banfield**¹⁵, **J. Boland**², **A. J. Brown**¹⁶, **J. Ceballos**¹⁷, **M. Dominguez-Pumar**¹⁸, **S. Espejo**¹⁷, **A. G. Fairén**^{1,12}, **R. Ferrandiz**¹, **E. Fischer**¹⁹, **M. Garcia-Villadangos**¹, **S. Gimenez**¹, **F. Gomez-Gomez**¹, **S. D. Guzewich**⁹, **A.-M. Harri**⁷, **J. J. Jimenez**⁸, **V. Jimenez**¹⁸, **T. Makinen**¹⁰, **M. Marin**¹, **C. Martin**¹⁰, **J. Martin-Soler**¹, **A. Molina**¹, **L. Mora-Sotomayor**¹, **S. Navarro**¹, **V. Peinado**¹, **I. Perez-Grande**²⁰, **J. Pla-Garcia**¹, **M. Postigo**¹, **O. Prieto-Ballesteros**¹, **S. C. R. Rafkin**²¹, **M. I. Richardson**⁶, **J. Romeral**¹, **C. Romero**¹, **H. Savijärvi**⁷, **J. T. Schofield**², **J. Torres**⁸, **R. Urqui**¹, **S. Zurita**¹ & **the MEDA team**^{*}

¹Centro de Astrobiología (INTA-CSIC), Madrid, Spain. ²Jet Propulsion Laboratory, California Institute of Technology, Pasadena, CA, USA. ³Dept. Física Aplicada, Universidad del País Vasco (UPV/EHU), Bilbao, Spain. ⁴Lunar and Planetary Institute, Houston, TX, USA. ⁵Space Science Institute, Boulder, CO, USA. ⁶Aeolis Corporation, Sierra Madre, CA, USA. ⁷Finnish Meteorological Institute, Helsinki, Finland. ⁸Instituto Nacional de Técnica Aeroespacial (INTA), Madrid, Spain. ⁹NASA Goddard Space Flight Center, Greenbelt, MD, USA. ¹⁰Dept. Física y Matemáticas, Universidad de Alcalá, Alcalá de Henares, Spain. ¹¹Institute of Physical Chemistry Rocasolano, CSIC, Madrid, Spain. ¹²Cornell University, Ithaca, NY, USA. ¹³Carnegie Institution, Washington, DC, USA. ¹⁴Institut Supérieur de l'Aéronautique et de l'Espace (ISAE-SUPAERO), Université de Toulouse, Toulouse, France. ¹⁵NASA Ames Research Center, Mountain View, CA, USA. ¹⁶Plancius Research, Severna Park, MD, USA. ¹⁷Instituto de Microelectrónica de Sevilla (US-CSIC), Sevilla, Spain. ¹⁸Dept. de Ingeniería Electrónica, Universidad Politécnica de Cataluña, Barcelona, Spain. ¹⁹Dept. of Climate and Space Sciences and Engineering, University of Michigan, Ann Arbor, MI, USA. ²⁰Dept. de Mecánica de Fluidos y Propulsión Aeroespacial, Universidad Politécnica de Madrid, Madrid, Spain. ²¹Southwest Research Institute, Boulder, CO, USA. ^{*}A full list of members and their affiliations appears at the end of the paper. ^{**}A full list of members and their affiliations appears in the Supplementary Information. ✉e-mail: manfredi@cab.inta-csic.es; manuel.delatorrejuarez@jpl.nasa.gov; agustin.sanchez@ehu.es;

the MEDA team

J. A. Rodriguez-Manfredi¹, **M. de la Torre Juarez**², **A. Sanchez-Lavega**³, **R. Hueso**³, **G. Martinez**⁴, **M. T. Lemmon**⁵, **C. E. Newman**⁶, **A. Manguira**³, **M. Hieta**⁷, **L. K. Tamppari**², **J. Polkko**⁷, **D. Toledo**⁸, **E. Sebastian**¹, **M. D. Smith**⁹, **I. Jaakonaho**⁷, **M. Genzer**⁷, **A. De Vicente-Retortillo**¹, **D. Viudez-Moreiras**¹, **M. Ramos**¹⁰, **A. Saiz-Lopez**¹¹, **A. Lepinette**¹, **R. J. Sullivan**¹², **J. Gomez-Elvira**¹,

V. Apestigue⁸, P. G. Conrad¹³, T. Del Rio-Gaztelurrutia³, I. Arruego⁸, D. Banfield¹⁵, J. Boland², J. Ceballos¹⁷, M. Dominguez-Pumar¹⁸, S. Espejo¹⁷, A. G. Fairén^{1,12}, R. Ferrandiz¹, E. Fischer¹⁹, M. Garcia-Villadangos¹, S. Gimenez¹, F. Gomez-Gomez¹, S. D. Guzewich⁹, A.-M. Harri⁷, J. J. Jimenez⁸, V. Jimenez¹⁸, T. Makinen⁷, M. Marin¹, C. Martin¹, J. Martin-Soler¹, A. Molina¹, L. Mora-Sotomayor¹, S. Navarro¹, V. Peinado¹, I. Perez-Grande²⁰, J. Pla-Garcia¹, M. Postigo¹, O. Prieto-Ballesteros¹, S. C. R. Rafkin²¹, M. I. Richardson⁶, J. Romeral¹, C. Romero¹, H. Savijärvi⁷, J. T. Schofield², J. Torres⁸, R. Urqui¹ & S. Zurita¹

A full list of members and their affiliations appears in the Supplementary Information.

Methods

MEDA operational strategy

MEDA can operate continuously and independently of the rover's battery charge cycles, 24 hours a day and subject to a measurement programme sent from Earth (Extended Data Fig. 1). The observation sessions are subject to power availability and, eventually, to incompatibility with other activities to be performed by the rover.

Due to these restrictions, the usual sequence of measurements that MEDA is carrying out consists of the acquisition of all the magnitudes that the instrument records every other hour. On the following sol, the measurement hours are reversed so that every two sols, a total coverage of all daily magnitudes is made.

TIRS measurements and analysis

The TIRS is an infrared radiometer with five channels that measure downward radiation (IR1), air temperature (IR2), reflected short-wave radiation (IR3), upward long-wave radiation (IR4) and ground temperature (IR5)². We use the ratio between TIRS IR3 and the 'total light' Top7 detector of the RDS (description follows) measurements as a proxy for surface albedo. Since TIRS and RDS measure in different bands, a correction is made using the COMIMART radiative transfer model¹².

TI can be straightforwardly derived across Perseverance's traverse by using MEDA values of the net heat flux into the ground as the upper boundary condition to solve the heat conduction equation for homogeneous terrains. This quantity governs the thermal amplitude in the shallow subsurface from diurnal to seasonal timescales, and therefore accurate estimations of TI can be useful to constrain the thermal environment of the samples collected by the Mars 2020 mission. For this estimation, numerical models need to simulate the SEB (see paragraphs that follow in this section). MEDA measures the SEB, allowing for a more in situ-based estimation of the TI.

Concerning TIRS infrared fluxes, the two upward-viewing sensors of TIRS (IR1 and IR2) enable the total column optical depth of aerosol above the rover to be retrieved. The observed signal in TIRS IR1 is sensitive to a combination of atmospheric temperatures and total aerosol optical depth (dust plus water-ice cloud). The atmospheric temperature profile is taken from concurrent observations by the interferometric thermal infrared spectrometer (EMIRS) instrument on board the Emirates Mars Mission⁴⁹ with temperatures near the surface modified to match the observed TIRS IR2 signal. A radiative transfer model including aerosol scattering is then used to find the aerosol optical depth that would produce the observed TIRS IR1 signal. The estimated uncertainty in these retrievals is ± 0.03 .

RDS measurements and analysis

The RDS comprises two sets of eight photodiodes (RDS-DP) and a camera (SkyCam)^{2,50}. One set of photodiodes is pointed upward, with each one covering a different wavelength range between 190 and 1,200 nm. The other set is pointed sideways, 20° above the horizon, and they are spaced 45° apart in azimuth to sample all directions at a single wavelength.

HS measurements and analysis

The HS provides directly the local RH and local sensor temperature. Combined with the pressure data provided by the MEDA pressure sensor (PS), water-vapour VMR can be calculated, too. The HS has two measurement modes: continuous measurement and high-resolution interval mode (HRIM). In HRIM, the HS is powered on for only 10 s and then powered off to avoid self-heating. HRIM provides the measurements with the best accuracy, but continuous measurements are beneficial for monitoring changes in RH during short periods.

PS measurements and analysis

The PS is actually a set of two capacitive transducers that provide the hydrostatic pressure as a function of the local temperature, for which the sensor also provides its own temperature².

They are the Barocaps RSP2M and NGM (due to the internal operation of the sensor, only one or the other can work, not both simultaneously), which can be operated at 0.5 or 1 Hz; the RSP2M has a worse resolution and worse stability than the NGM, but the RSP2M's warm-up time is shorter.

Atmospheric temperature sensor measurements and analysis

Atmospheric temperature sensors (ATSs) are thin thermocouple sensors with three sensors distributed azimuthally around the remote-sensing mast (RSM) at an altitude of 1.45 m and two sensors on the front sides of the rover at an altitude of 0.85 m, which can provide local temperature measurements at a configurable rate. The location of three sensors around the RSM ensures that at least one of them is located downwind during most of the time, producing a clean measurement of air temperature. The two sensors at 0.85 m are more shielded from the environment.

A systematic comparison of ATS data and wind measurements, including the rover orientation on each individual sol, guided us to use the following rules to select the appropriate ATS to characterize the unperturbed atmosphere. During daylight hours, the sensor at $z = 1.45$ m measuring the lowest temperature is generally the one located downwind. In certain wind conditions, two sensors can be located downwind, and they show very similar temperatures (within 0.1 K) and equivalent oscillations. At $z = 0.85$ m during daylight hours, we select the sensor with the lowest temperature. To take into account changes in wind direction that modify the selected ATS, we consider slow transitions from one sensor to another at each level when the sensor measuring the lowest temperature changes. During night-time, the smaller values of the winds and the sheltered location of the two ATSs at $z = 0.85$ m typically result in one sensor generally much warmer than the other. Comparison with environment winds indicates that the lowest temperature sensor is always the most exposed to environment winds with the lowest thermal perturbations from the rover. In the RSM, all three ATSs can experience radiative cooling effects from the rover deck. Thus, when two ATSs have highly correlated values and thermal oscillations, we use the average of them instead of the ATS with the lowest temperature. Thermal perturbations from the radioisotope thermal generator are easily observed at night at $z = 1.45$ m and identified from the wind data and rover orientation and do not have any noticeable effect on the results here presented. The radioisotope thermal generator, located at the back of the rover, does not generally cause detections in the sheltered detectors in the front of the rover at $z = 0.85$ m.

Wind measurements and analysis

The wind sensor consists of two horizontal booms placed on the RSM 1.5 m above the rover base and rotated in azimuth 120° with respect to each other.

This placement allows at least one of them to be out of thermal disturbance and out of the rover geometry for any wind direction. Therefore, the level of confidence and the analysis of the perturbing effect that the rover causes on the measurements made will properly depend on the wind direction and speed.

Thus, the data retrieval procedure implemented on the ground consists of the weighted combination of the local wind-speed retrievals from each individual sensor, thereby obtaining the free-flow wind estimate. The weighting of each contribution is established on the basis of the results of the computational fluid dynamic models developed to evaluate how the free wind flow is affected by the rover hardware, thus allowing interpretation of the local wind measurements at each boom location. More details of this process are provided in ref. 2.

SkyCam image analysis

The SkyCam imager is integrated inside the RDS sensor (described in the preceding) and permanently pointed at the Martian sky. The orientation of the camera is not motorized, and its optics are fixed.

SkyCam optical depths were measured via extinction determined through direct solar imaging². The image field of view includes an annular ND-5 coating: when the Sun is within that coated region twice each sol, it appears comparable in brightness to the sky outside the annulus. Flux from the Sun was integrated after removal of background signal (mostly dark current). From the flux and atmospheric path at the time of each image, optical depth is calculated as $\tau = \ln(F/F_0)/\eta$, where τ is normal optical depth, F is observed solar flux, F_0 is a calibration parameter representing solar flux in the absence of an atmosphere and η is air mass, which is the ratio of atmospheric column mass on the observed ray to normal column mass. Because SkyCam cannot be calibrated by observing a wide range of air masses or changing the camera versus atmosphere geometry⁴⁰, it was calibrated by comparison with MastCam-Z-derived optical depths²².

The current estimates of SkyCam opacity uncertainties are 0.07, while those for AM–PM differences are 0.08, and neither varies much among points. The variation among AM–PM differences is not substantial for sols 50–250. However, the population average is 0.10 ± 0.01 for sols 50–250 and -0.01 ± 0.04 before sol 50.

Derivation and importance of SEB

MEDA enables in situ quantification of the SEB on Mars. To this end, conservation of energy at the surface–atmosphere interface of Mars requires that

$$G = (SW_d - SW_u) + (LW_d - LW_u) + T_f - L_f \quad (1)$$

where G represents the net heat flux into the ground, SW_d is the downwelling solar flux, SW_u is the solar flux reflected by the surface, LW_d is the downwelling long-wave atmospheric flux, LW_u is the upwelling long-wave flux emitted by the surface, T_f is the turbulent heat flux and L_f is the latent heat flux. By convention, radiative fluxes directed towards the surface (warming) and nonradiative fluxes (T_f , L_f , and G) directed away from the surface (cooling) are taken as positive in equation (1). Moreover, the radiative fluxes are plugged into equation (1) as positive values, whereas nonradiative fluxes can be plugged in as positive or negative depending on whether they are directed away from or towards the surface.

RDS measures SW_d between 0.2 and 1.2 μm , while TIRS measures SW_u between 0.3 and 3 μm and LW_d and LW_u between 6.5 and 30 μm ^{2,52,53}. As required in quantifications of the SEB, measured radiative fluxes must be extended to the entire short-wave (0.2–5 μm) and long-wave (5–80 μm) ranges. To extend SW_d and SW_u , we use the radiative transfer model COMIMART¹² along with measured values of aerosol optical depth from the MastCam-Z instrument²². We note that the incoming radiation between 0.2 and 1.2 μm accounts for around 78% of the entire short-wave flux and that the uncertainty in this extension is small because COMIMART includes wavelength-dependent dust radiative properties, accounting for the variations (smaller than 3% for the majority of conditions) in the conversion factor as a function of dust opacity and solar zenith angle. Similarly, we assume a surface emissivity, ϵ , of 0.99 and the Stefan–Boltzmann law to extend LW_u . This value of ϵ minimizes the difference between the ground temperature measured by TIRS (8–14 μm) and the ground temperature derived from LW_u . To extend LW_d , we use the University of Helsinki/Finnish Meteorological Institute adsorptive subsurface–atmosphere single column model (SCM) along with measured values of aerosol optical depth⁵¹. Figure 1a shows the diurnal evolution of each term of the SEB terms on a particular sol, both obtained from MEDA (symbols) and simulated by SCM (solid lines). Extended Data Fig. 2 shows the evolution of these magnitudes recorded by MEDA over the first 250 sols. The excellent agreement demonstrates that MEDA's measurements are robust.

The turbulent heat flux is defined as $T_f = \rho_a c_p \overline{w'T'}$, where ρ_a is the air density, $c_p = 736 \text{ J kg}^{-1} \text{ K}^{-1}$ is the specific heat of CO_2 gas at constant pressure and $\overline{w'T'}$ is the covariance between turbulent departures of

the vertical wind speed, w' , and temperature, T' . These departures are typically calculated over periods of about a few minutes¹⁶. As MEDA measurements of w are not yet available, we use the drag transfer method⁵⁴ to indirectly calculate the turbulent heat flux as:

$$T_f = k^2 U_a \rho_a c_p f(R_B) \frac{(T_g - T_a)}{\ln^2(z_a/z_0)} \quad (2)$$

where $k = 0.4$ is the von Karman constant, $z_a = 1.45 \text{ m}$ is the height at which the air temperature and horizontal wind speed (U_a) are measured, z_0 is the surface roughness (set to 1 cm (ref. 55)) and $f(R_B)$ is a function of the bulk Richardson number that accounts for the thermal stability in the near surface of Mars⁵⁶.

We note that L_f has been neglected in the SEB because formation or sublimation of surface ice has not been detected at Jezero to date, with maximum near-surface relative humidity values below 25% for the first 250 sols.

Derivation of thermal inertia using MEDA measurements

We use MEDA measurements of the SEB as the upper boundary condition to solve the heat conduction equation in the soil for homogeneous terrains:

$$\frac{\partial T(z, t)}{\partial t} = \left(\frac{\text{TI}}{\rho c_p} \right)^2 \frac{\partial^2 T(z, t)}{\partial z^2} \quad (3)$$

$$-\frac{\text{TI}}{\rho c_p} \frac{\partial T(z=0, t)}{\partial z} = G = (SW_d - SW_u) + (LW_d - LW_u) + T_f - L_f \quad (4)$$

$$T(z = z_d, t) = T_d, \quad (5)$$

where TI is the thermal inertia, ρ is the soil density, c is the soil specific heat and z_d is the depth at which the subsurface temperature is constant and equal to T_d . Here we assume that $\rho_c = 1.2 \times 10^6 \text{ J m}^{-3} \text{ K}^{-1}$ and $z_d = 3 \times L$, where $L = \left(\frac{\text{TI}}{\rho c} \right) \sqrt{\frac{2}{\omega}}$ is the diurnal e-folding depth and $\omega = 7.0774 \times 10^{-5} \text{ s}^{-1}$ is the angular speed of Mars's rotation.

Under these assumptions, T_d and TI are the only unknowns, which can be solved by best fitting the solution to equations (3)–(5) to measured values of the daily minimum ground temperature and diurnal amplitude in ground temperature, respectively. As analysed in ref. 54, the solution to equations (3)–(5) depends primarily on TI, with considerably smaller variations as a function of T_d , z_d and ρ_c .

Derivation of albedo using MEDA measurements

We calculate the broadband albedo in the 0.3–3.0 μm range as

$$\alpha = SW_u^{0.3-3\mu\text{m}} / SW_d^{0.3-3\mu\text{m}} \quad (6)$$

Here, $SW_u^{0.3-3\mu\text{m}}$ is the reflected solar flux measured directly by TIRS, while $SW_d^{0.3-3\mu\text{m}}$ is the downwelling solar flux calculated with COMIMART by extending RDS Top7 measurements from 0.19–1.20 to 0.3–3.0 μm . On the basis of uncertainties in measured solar fluxes, the relative error in albedo is <10% in the vicinity of noon and <20% towards sunset and sunrise.

Description of COMIMART and UH/FMI SCM

COMIMART includes wavelength-dependent radiative properties of the Martian atmospheric constituents. Dust radiative properties are calculated from the refractive indices derived from satellite observations^{32,57}. We have assumed a dust particle effective radius of 1.5 μm and an effective variance of 0.3. The surface albedo is also assumed to depend on wavelength, with low values in the ultraviolet, increasing towards the near-infrared spectral region⁵⁸. However, this value barely

impacts simulations of downwelling solar fluxes. Solar radiative fluxes are calculated using the delta-Eddington approximation⁵⁹. The model has been validated for different solar elevations, dust abundances and scattering regimes¹², concluding that it is accurate for the majority of conditions that can be found at Jezero crater.

Unlike COMIMART, the University of Helsinki/Finnish Meteorological Institute single-column model (UH/FMISCM) allows the simulation of long-wave fluxes. SCM handles solar (short-wave) radiation with a fast broadband delta-two-stream approach for CO₂ and dust, and thermal (long-wave) radiation with a fast broadband emissivity approach for CO₂, H₂O and dust. These two schemes have been validated through comparisons from a multiple-scattering resolving model⁶⁰. As in COMIMART, dust optical parameters were obtained using refractive indices in refs. 32,57. This confirmed the dust SW single-scattering albedo to 0.90 and the asymmetry parameter to 0.70, which are used in our reference model.

When initialized with aerosol opacities retrieved from MastCam-Z at 880 nm, COMIMART and SCM simulate nearly identical solar fluxes, with relative departures <5% at noon.

Retrieval of dust scattering properties

Dust optical properties are estimated by simulating the RDS measurements² throughout the sol, using radiative transfer simulations. The irradiance (E) measured by a given RDS channel is computed as:

$$E = C \times [T(\mu_0, \varphi_0) \times e^{-\tau} + \int_0^{2\pi} \int_{-1}^0 I(\tau, \mu_0, \varphi_0, \mu, \varphi) \times T(\mu, \varphi) \times R \times \mu \times d\mu d\varphi] \quad (7)$$

where I is the scattered intensity simulated with a radiative transfer model, μ_0 and φ_0 are the cosine of the solar zenith angle and the solar azimuth angle, μ and φ are the cosine of the zenith angle and the azimuth angle of the observation, T and R are the sensor angular response and responsivity, C is a constant and τ is the total vertical opacity. Extended Data Fig. 10a shows RDS Top5 (750 nm) signals simulated for different dust opacities and an effective radius of $r_{\text{eff}} = 1.2 \mu\text{m}$.

Here we see that, by varying the dust opacity, the simulated signals change in value and shape. Similar results are found when we vary the effective radius of the particles, keeping constant the dust number density. By changing r_{eff} , we vary the dust opacity through the particle cross section, the particle phase function and the single-scattering albedo. Estimation of the free parameters (for example dust number density or dust particle radius) is performed by finding the optimal value of the parameter that minimizes the differences between observations and simulations, as shown in Extended Data Fig. 10b, using the Levenberg–Marquardt procedure.

The dust particle radius is estimated using (1) the observations made by the RDS lateral photodiodes², whose FoV is narrow ($\pm 5^\circ$), when the Sun is near the FoV of one of those detectors (this occurs when the Sun is at low elevation); at that time, RDS lateral detectors provide observations at a wide range of scattering angles (sensitive to the particle phase function); (2) the observations made by the top photodiodes at different wavelengths (for example, 450, 650, 750, 950 nm). In this case, the opacity at each channel wavelength depends on the particle radius, so by fitting the observations made at different wavelengths simultaneously, we can derive the size of the dust particles. To better constrain the particle radius, the observations from RDS and SkyCam can be combined: the opacity derived from SkyCam can be used when fitting the observations made by RDS, being in this case the particle radius is the only free parameter in the retrieval.

Once the particle radius is estimated, we can provide the dust opacity at different time intervals, such as the daily or the hourly average, by assuming the particle radius does not change much throughout the sol.

Data availability

All datasets of Mars 2020 are available via the Planetary Data System (PDS). Data are delivered to the PDS according to the Mars 2020 Data

Management Plan available in the Mars 2020 PDS archive (<https://doi.org/10.17189/1522849>). Data from the MEDA instrument referenced in this paper are available from the PDS Atmospheres node. The direct link is https://pds-atmospheres.nmsu.edu/data_and_services/atmospheres_data/PERSEVERANCE/meda.html.

References

- Edwards, C. S. et al. The Emirates Mars Mission (EMM) Emirates Mars infrared spectrometer (EMIRS) instrument. *Space Sci. Rev.* **217**, 77 (2021).
- Apestigue, V. et al. Radiation and dust sensor for Mars Environmental Dynamics Analyzer onboard M2020 rover. *Sensors* **22**, 2907 (2022).
- Savijärvi, H. I. et al. Humidity observations and column simulations for a warm period at the Mars Phoenix lander site: constraining the adsorptive properties of regolith. *Icarus* **343**, 113688 (2020).
- Sebastian, E. et al. Radiometric and angular calibration tests for the MEDATIRS radiometer onboard NASA's Mars 2020 mission. *Measurement* **164**, 107968 (2020).
- Sebastián, E. et al. Thermal calibration of the MEDA-TIRS radiometer onboard NASA's Perseverance rover. *Acta Astronaut.* **182**, 144–159 (2021).
- Martínez, G. M. et al. Surface energy budget and thermal inertia at Gale Crater: calculations from ground-based measurements. *J. Geophys. Res. Planets* **119**, 1822–1838 (2014).
- Hébrard, E. et al. An aerodynamic roughness length map derived from extended Martian rock abundance data. *J. Geophys. Res. Planets* <https://doi.org/10.1029/2011je003942> (2012).
- Savijärvi, H. & Kauhanen, J. Surface and boundary-layer modelling for the Mars Exploration Rover sites. *Q. J. R. Meteorol. Soc. A* **134**, 635–641 (2008).
- Wolff, M. J., Clancy, R. T., Goguen, J. D., Malin, M. C. & Cantor, B. A. Ultraviolet dust aerosol properties as observed by MARCI. *Icarus* **208**, 143–155 (2010).
- Mustard, J. F. & Bell, J. F. III New composite reflectance spectra of Mars from 0.4 to 3.14 μm . *Geophys. Res. Lett.* **21**, 353–356 (1994).
- Joseph, J. H., Wiscombe, W. J. & Weinman, J. A. The delta-Eddington approximation for radiative flux transfer. *J. Atmos. Sci.* **33**, 2452–2459 (1976).
- Savijärvi, H., Crisp, D. & Harri, A.-M. Effects of CO₂ and dust on present-day solar radiation and climate on Mars. *Q. J. R. Meteorol. Soc.* **131**, 2907–2922 (2005).

Acknowledgements

This work has been funded by the Spanish Ministry of Economy and Competitiveness, through the projects no. ESP2014-54256-C4-1-R (also -2-R, -3-R and -4-R); Ministry of Science, Innovation and Universities, projects no. ESP2016-79612-C3-1-R (also -2-R and -3-R); Ministry of Science and Innovation/State Agency of Research (10.13039/501100011033), projects no. ESP2016-80320-C2-1-R, RTI2018-098728-B-C31 (also -C32 and -C33), RTI2018-099825-B-C31, PID2019-109467GB-I00 and PRE2020-092562; Instituto Nacional de Técnica Aeroespacial; Ministry of Science and Innovation's Centre for the Development of Industrial Technology; Spanish State Research Agency (AEI) Project MDM-2017-0737 Unidad de Excelencia “María de Maeztu”—Centro de Astrobiología; Grupos Gobierno Vasco IT1366-19; and European Research Council Consolidator Grant no 818602. The US co-authors performed their work under sponsorship from NASA's Mars 2020 project, from the Game Changing Development programme within the Space Technology Mission Directorate and from the Human Exploration and Operations Directorate. Part of this research was carried out at the Jet Propulsion Laboratory, California Institute of Technology, under a contract with the National Aeronautics and Space Administration (80NMO018D0004). G.M. acknowledges

JPL funding from USRA Contract Number 1638782. A.G.F. is supported by the European Research Council, Consolidator Grant no. 818602.

Author contributions

J.A.R.-M. is the principal investigator of the MEDA instrument; together with M.d.I.T.J. and A. Sanchez-Lavega, the three are the corresponding authors of this manuscript. These corresponding authors have led the review and editing of the document. In addition, all authors have contributed to the conceptualization of the instrument and of this work. J.A.R.-M., M.d.I.T.J., A. Sanchez-Lavega, M.G., I.A., A.-M.H., L.M.-S., V.P. and R.U. have contributed to obtaining and managing the resources that have made this work possible. J.A.R.-M., M.d.I.T.J., A. Sanchez-Lavega, R.H., G.M., M.T.L., C.E.N., A. Manguira, M.H., L.K.T., J.P., D.T., E.S., M.D.S., I.J., M.G., A.D.V.-R. and D.V.-M. have participated in the writing of this manuscript, as well as M.R., A. Saiz-Lopez, A.L., M.W., R.J.S., J.G.-E., V.A., P.G.C., T.D.R.-G., N.M., A.J.B., D.B., A.G.F., E.F. and S.N., who contributed to the revision of the document in its different stages. J.A.R.-M., M.d.I.T.J., A. Sanchez-Lavega, R.H., G.M., M.T.L., C.E.N., L.K.T., D.T., E.S., J.G.-E., V.A. and J.T.S. defined the corresponding methodology. J.A.R.-M., M.d.I.T.J., A. Sanchez-Lavega, R.H., G.M., M.T.L., C.E.N., A. Manguira, M.H., L.K.T., J.P., D.T., E.S., M.D.S., I.J., A.D.V.-R., D.V.-M., A.L., M.W., J.G.-E., V.A., N.M., M.D.-P., A.G.F., E.F., S.D.G., A.-M.H., M.M., S.N., J.P.-G., S.C.R.R., M.I.R. and H.S. are involved on a daily basis with analysis of the recorded data. J.A.R.-M., M.d.I.T.J., R.H., G.M., M.T.L., C.E.N., A. Manguira, L.K.T., D.T., M.D.S., A.D.V.-R., D.V.-M., A.L., M.W., R.J.S., V.A., P.G.C., N.M., D.B., E.F., S.G., F.G.-G., M.M., C.M., A. Molina, L.M.-S., S.N., V.P., J.P.-G., C.R., J.T., R.U. and S.Z.

participated in the operation of the instrument. J.A.R.-M., M.d.I.T.J., G.M., M.T.L., M.H., L.K.T., D.T., E.S., M.D.S., A.L., J.G.-E., V.A., J.B., J.C., M.D.-P., S.E., E.F., J.J.J., M.M., J.M.-S., L.M.-S., S.N., V.P., J.R. and J.T. took part in the curation and validation of data.

Competing interests

The authors declare no competing interests.

Additional information

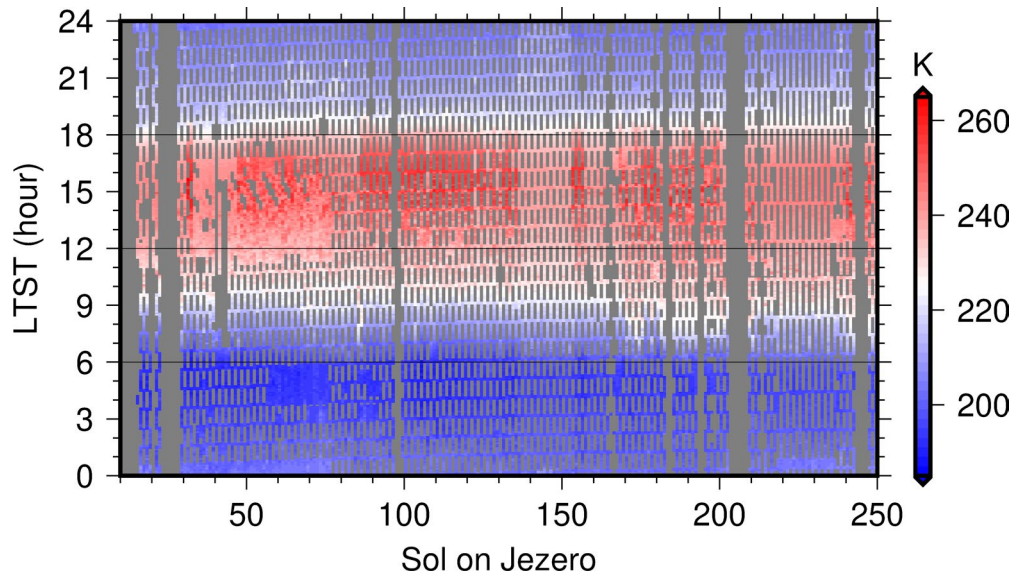
Extended data is available for this paper at <https://doi.org/10.1038/s41561-022-01084-0>.

Supplementary information The online version contains supplementary material available at <https://doi.org/10.1038/s41561-022-01084-0>.

Correspondence and requests for materials should be addressed to J. A. Rodriguez-Manfredi, M. de la Torre Juarez or A. Sanchez-Lavega.

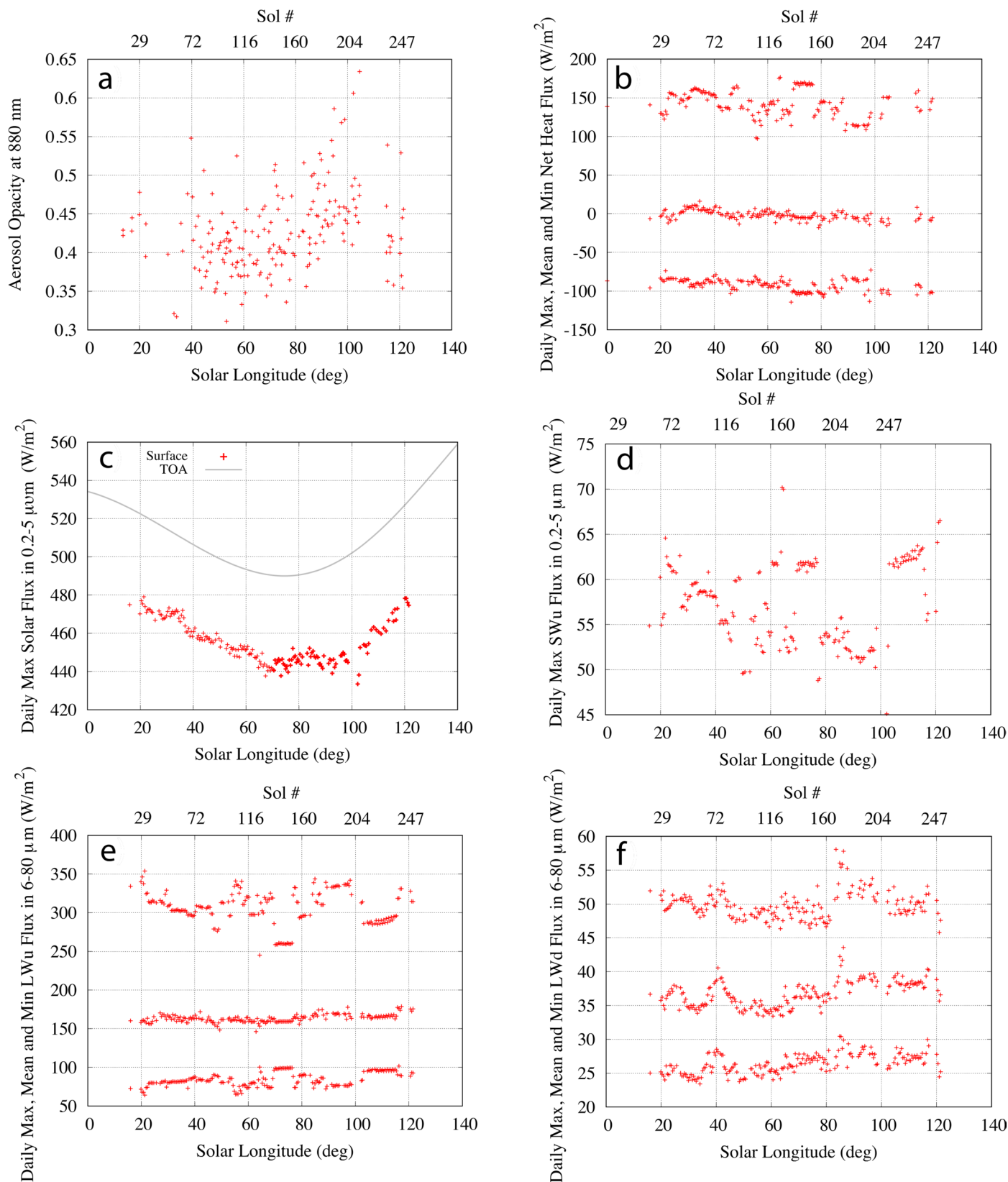
Peer review information *Nature Geoscience* thanks Jim Murphy and Peter Read for their contribution to the peer review of this work. Primary Handling Editor: Tamara Goldin, in collaboration with the *Nature Geoscience* team.

Reprints and permissions information is available at www.nature.com/reprints.



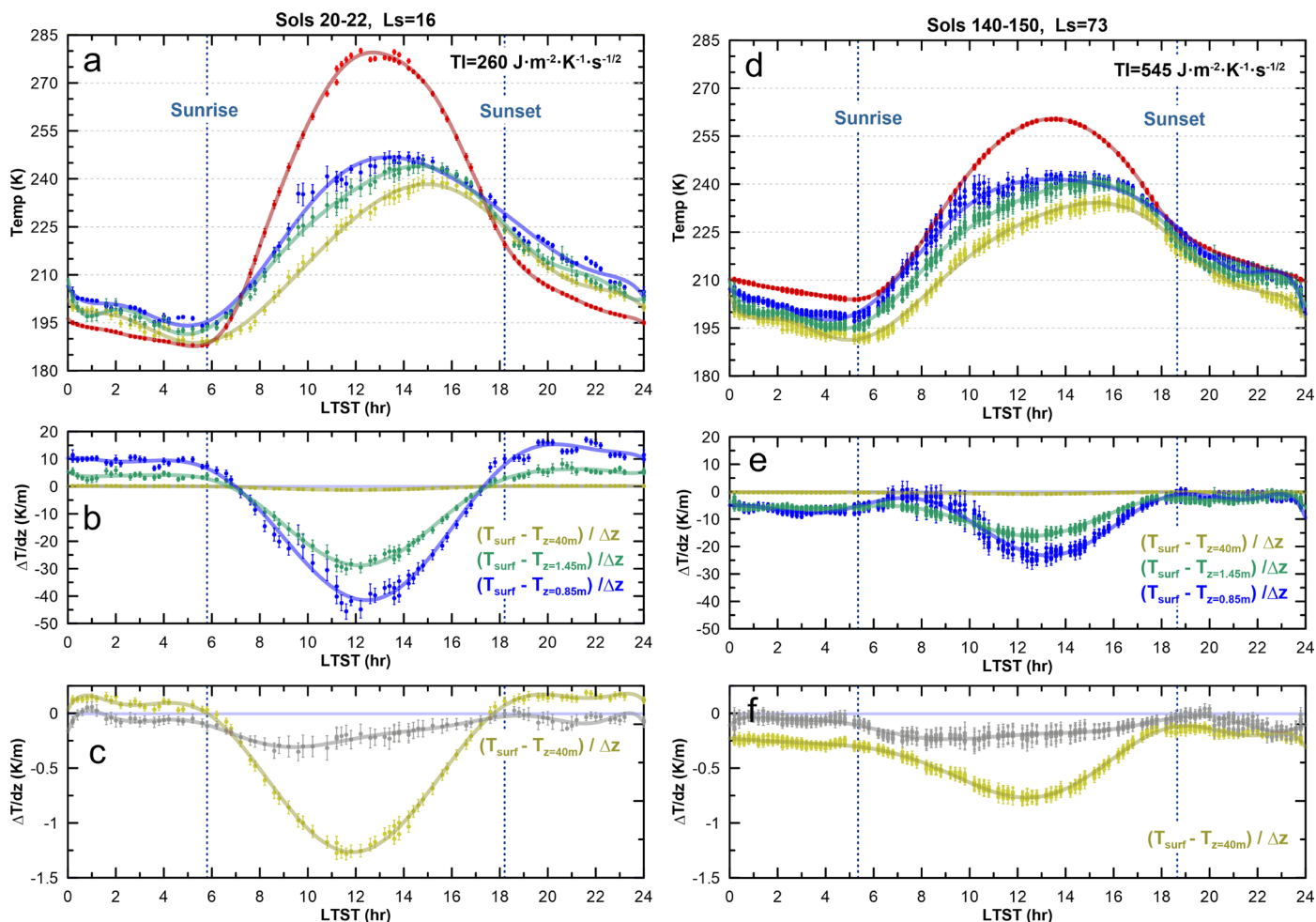
Extended Data Fig. 1 | MEDA's Temporary coverage during the first sols on Mars. Temporary coverage during the first few sols of Perseverance on the surface of Mars showing, as an example, one of the magnitudes recorded by the instrument. Blank periods correspond to situations of mission necessity

(start-up, software updates, etc.), or to a specific incident that has occurred to the instrument. The color code corresponds to the temperature recorded by the air temperature sensor (ATS) at $z = 1.45$ m, averaged every 5 minutes.



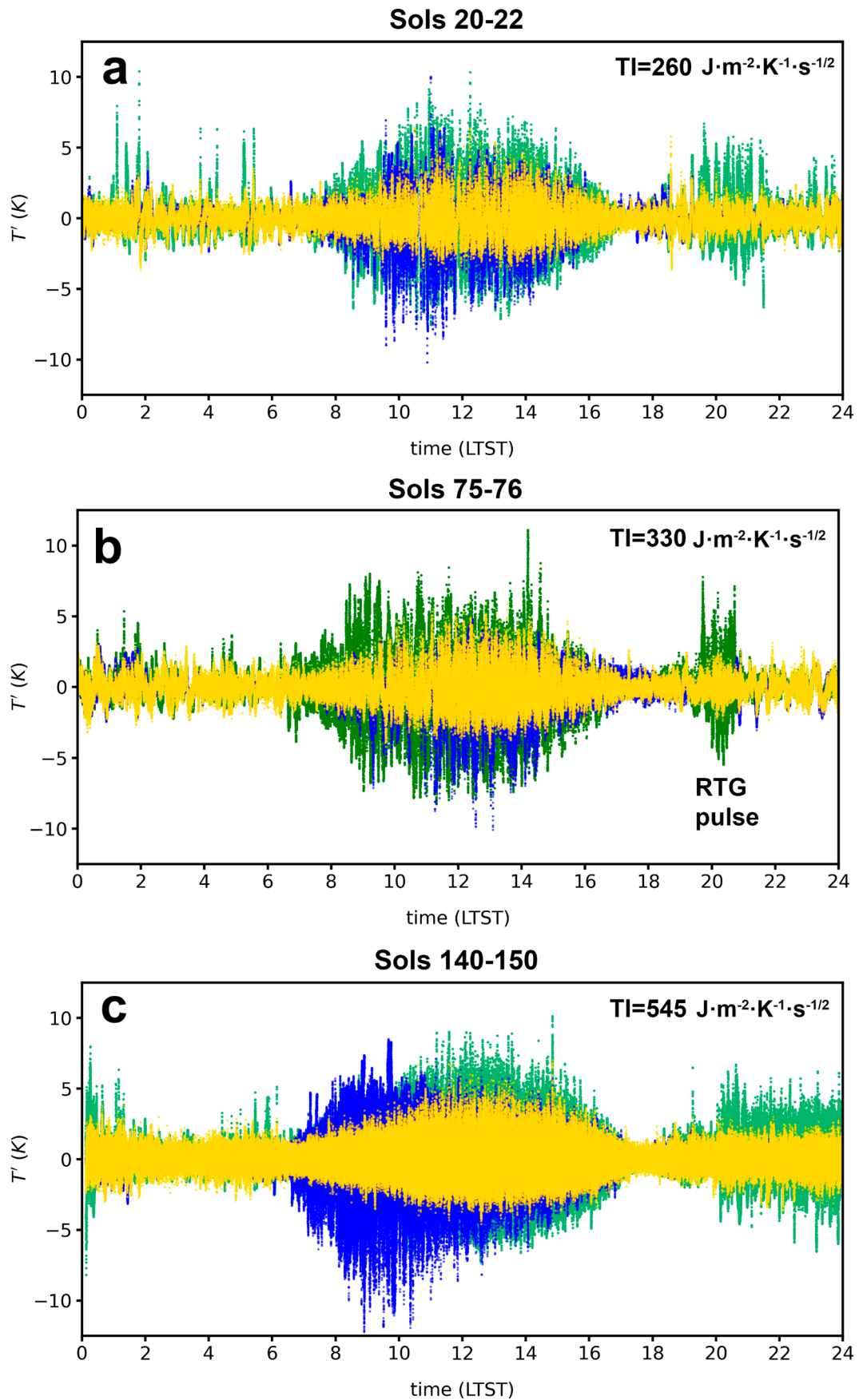
Extended Data Fig. 2 | Seasonal evolution of the SEB terms over the first 250 sols on Mars, as recorded by MEDA. Seasonal evolution for the first 250 sols of the M2020 mission of (a) The atmospheric opacity at 880 nm retrieved from MastCam-Z between 06:00 and 18:00 LMST. (b) Daily maximum, mean and minimum values of the net heat flux into the soil (G). (c) Daily maximum downwelling solar flux in the $0.2-5 \mu m$ range (SWd) at the surface (red) and at the top of the atmosphere (gray). The seasonal evolution of SWd at the surface

is governed by that the top of the atmosphere during the aphelion season, when the aerosol opacity is low and relatively stable. (d) Daily maximum solar flux in the $0.2-5 \mu m$ range reflected by the surface (SW_u). (e) Daily maximum upwelling longwave flux in the $6-80 \mu m$ range emitted by the surface (LW_u). (f) Daily maximum downwelling atmospheric longwave flux in the $6-80 \mu m$ range (LW_d). All these values were calculated as described in the Methods section.



Extended Data Fig. 3 | Daily cycle temperatures under typical values of thermal inertia and atmosphere's thermal gradients. Daily Cycle of temperatures at Jezero under low and high values of TI of the local terrain, and thermal gradients of the atmosphere. **(a-c)** Low thermal inertia with $TI = 260 \text{ J}\cdot\text{m}^{-2}\cdot\text{K}^{-1}\cdot\text{s}^{-1/2}$, as in sols 20-22. **(d-f)** High thermal inertia terrain with $TI = 545 \text{ J}\cdot\text{m}^{-2}\cdot\text{K}^{-1}\cdot\text{s}^{-1/2}$, as in sols 140-150. Colors legend is as in Fig. 2. Low surface thermal inertia

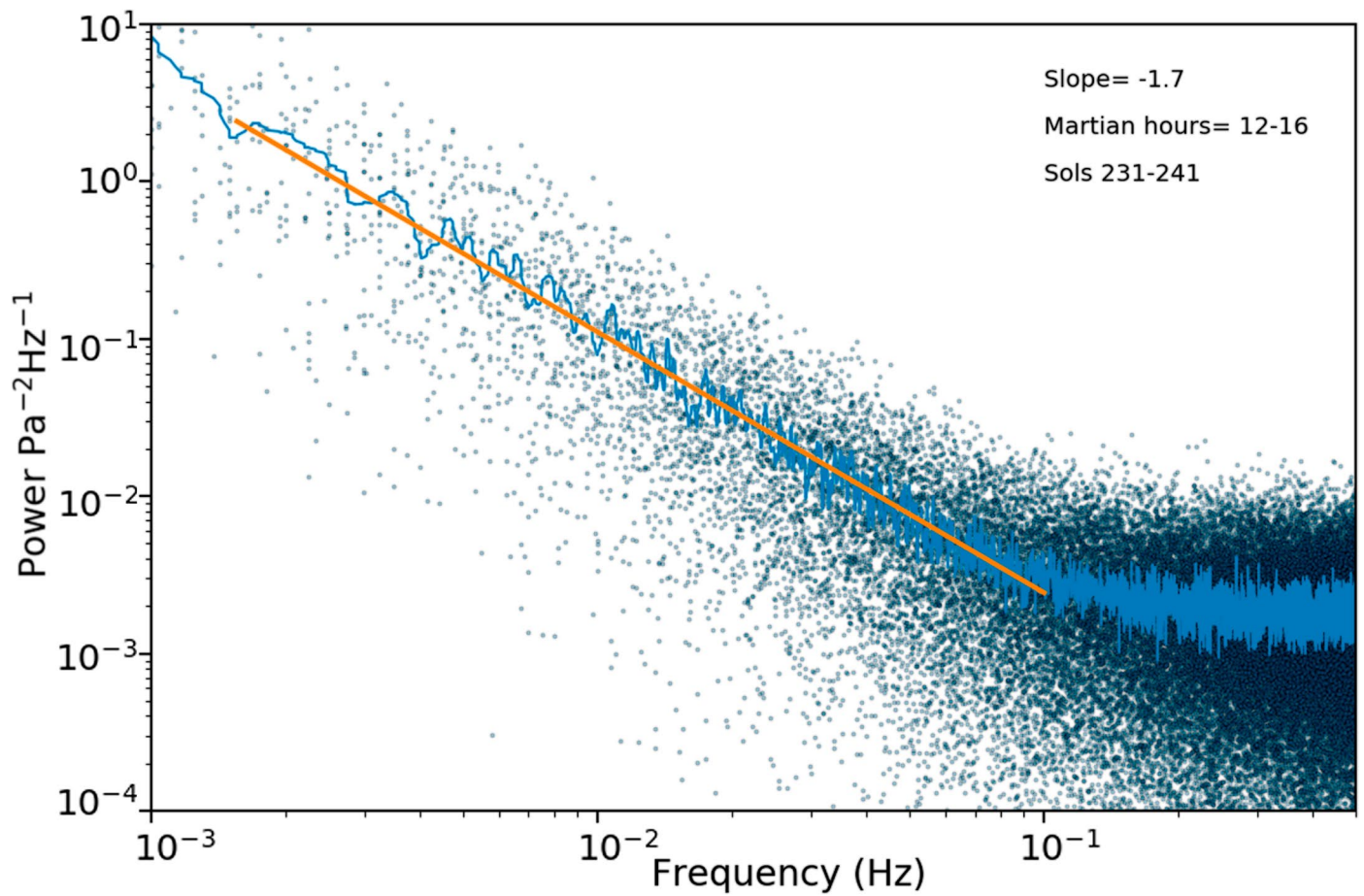
(left panels) result in more stable conditions with respect to vertical motions during nighttime than high values of the surface thermal inertia. This is due to the strong locality of surface temperatures, which change strongly in different terrains, compared to a more regular behavior of air temperatures (a and d). The data shown in these figures are the result of averaging the values over 12-minute time intervals, with the standard deviation as the error bar.



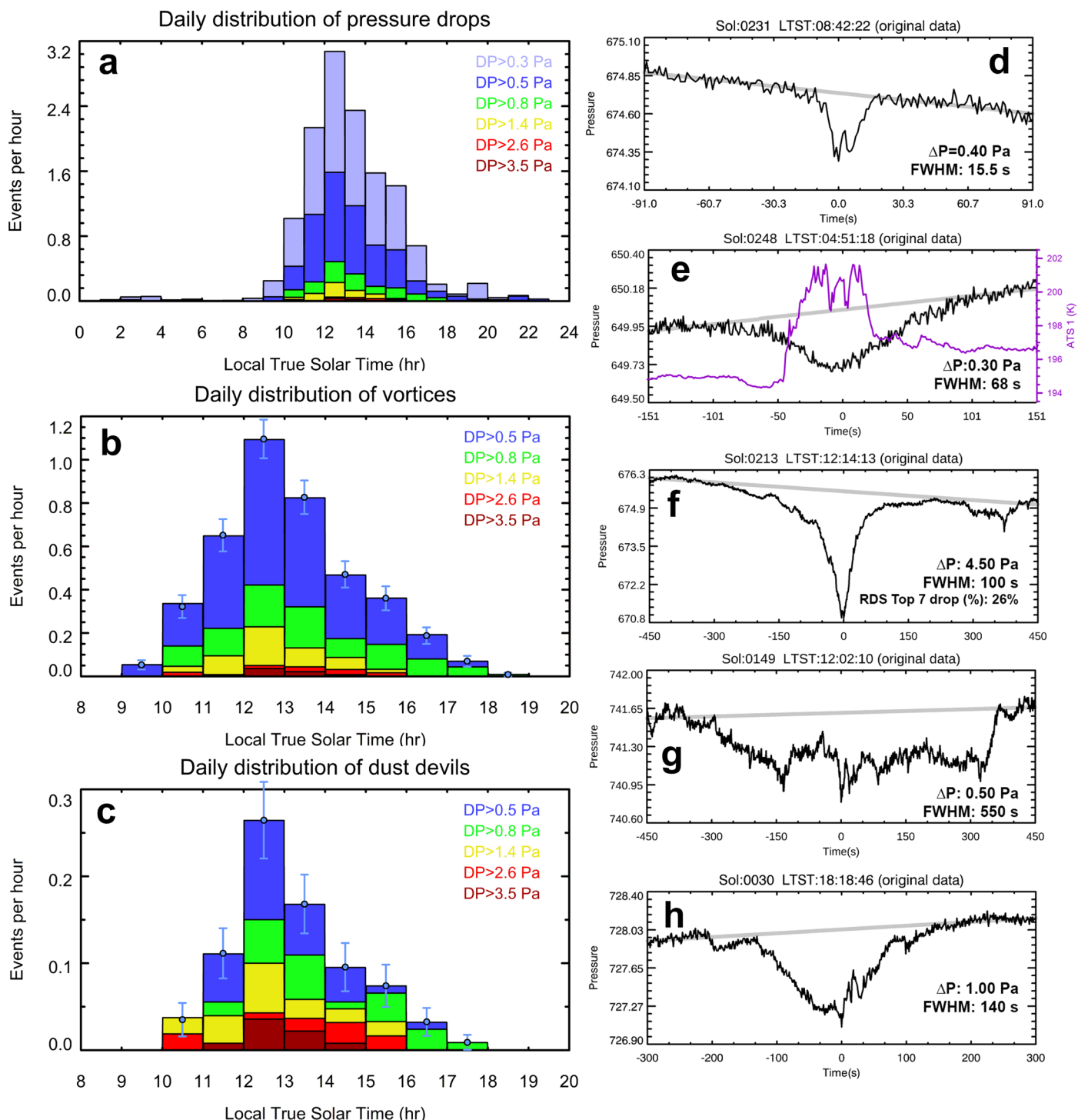
Extended Data Fig. 4 | See next page for caption.

Extended Data Fig. 4 | Analysis of thermal oscillations along the sols. Analysis of thermal oscillations along the sol, for the periods **(a)** sols 20-22, **(b)** sols 75-76, **(c)** sols 140-150, corresponding to different TI values. Blue dots correspond to ATS measurements at $z = 0.84$ m, green dots to ATS measurements at $z = 1.45$ m, and yellow dots to TIRS measurements at $z = -40$ m.

The large amplitudes around 20:00 h correspond to thermal contamination by the RTG at that time, as confirmed by simultaneous wind and rover yaw. The oscillations were calculated by detrending the temperature data in each half-hour period using a 2nd order polynomial.

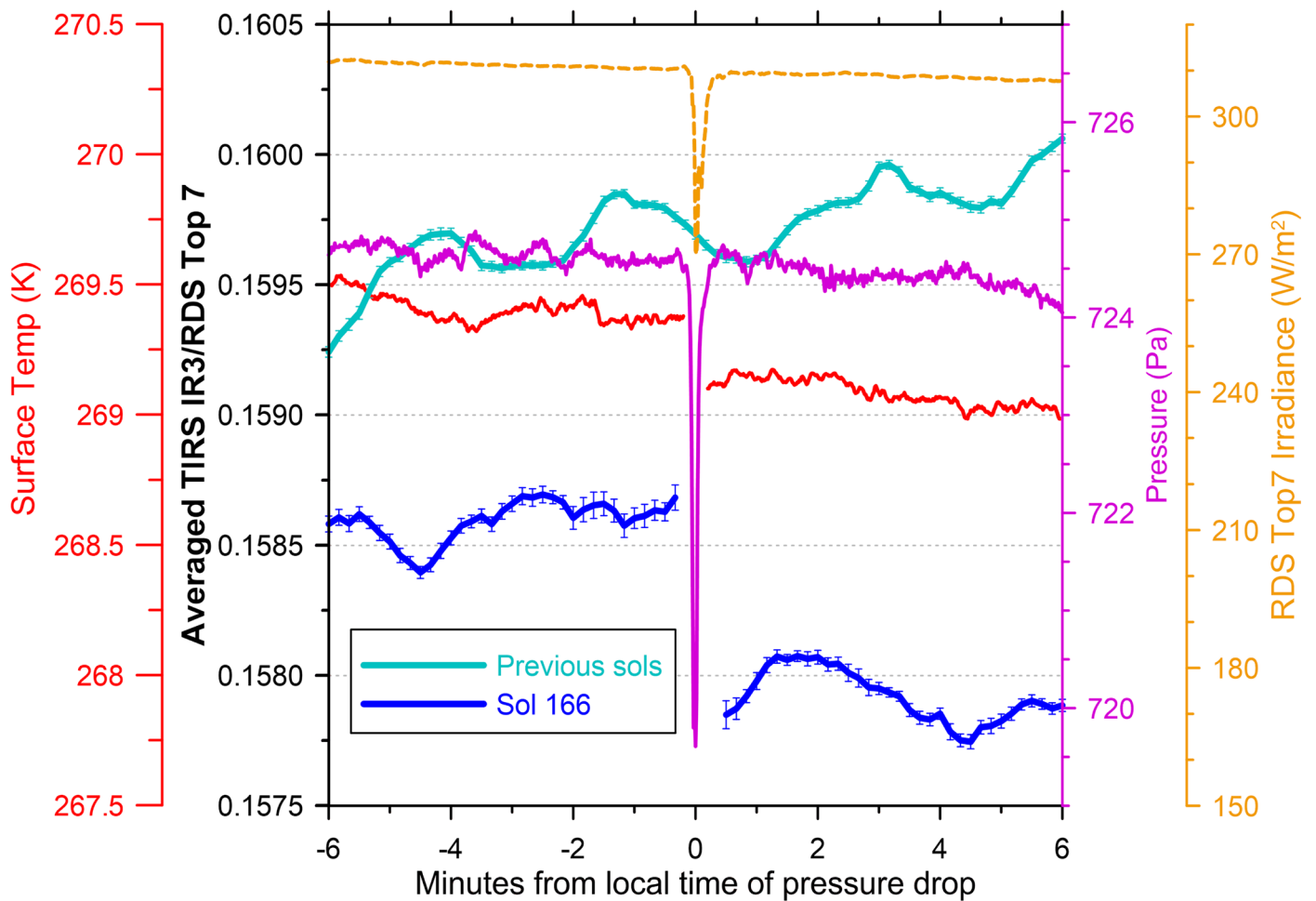


Extended Data Fig. 5 | Analysis of the rapid pressure fluctuations. Power spectrum of pressure fluctuations from sols 231 to 241. The straight line determines the power law fit in the frequency range 0.001 to 0.1 Hz.



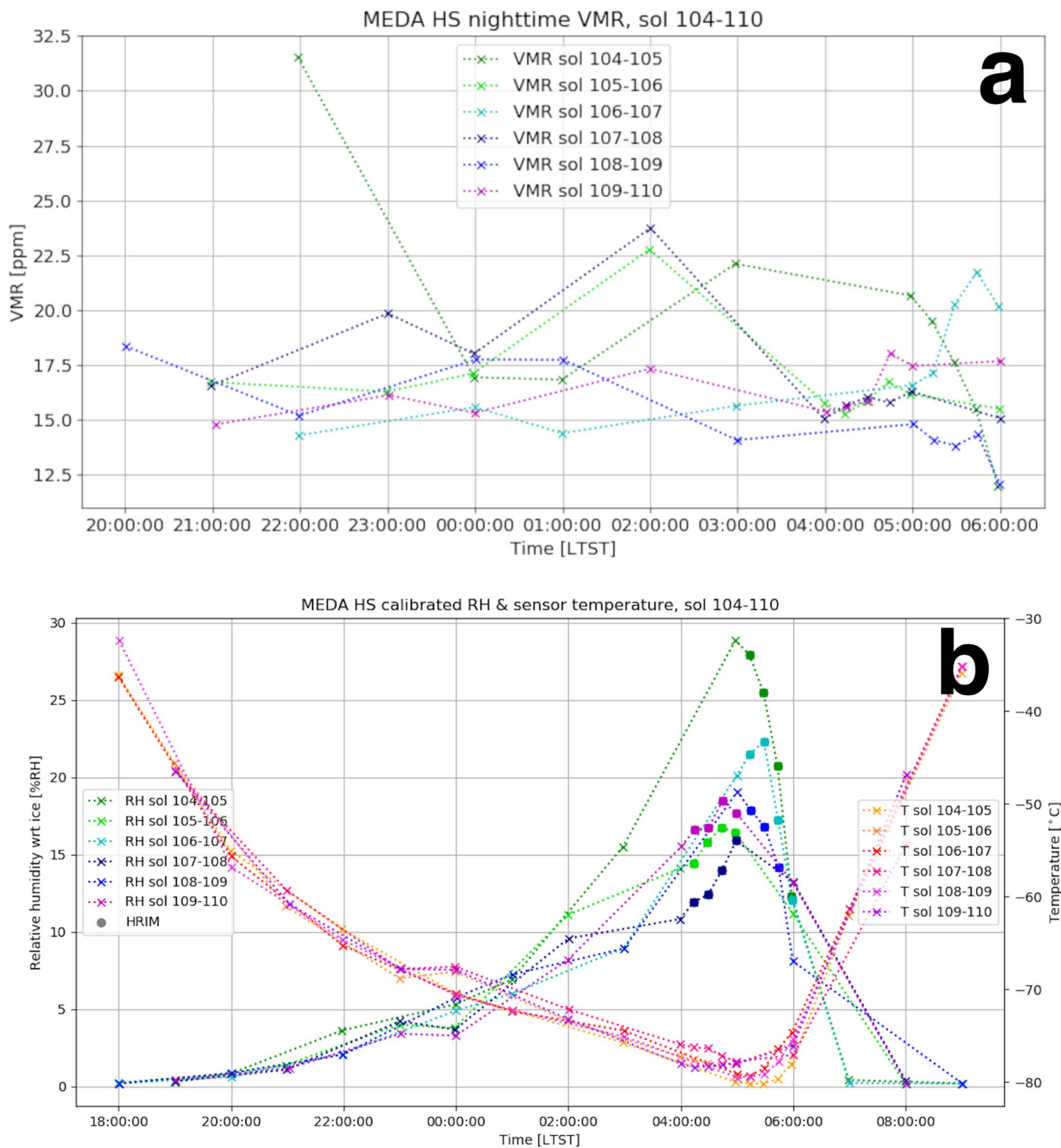
Extended Data Fig. 6 | Pressure drops as observed by MEDA. Pressure drops on MEDA data. **(a)** Daily distribution of pressure drops identified using the algorithm described in¹⁴. **(b)** Selection of events with at least a pressure drop of 0.5 Pa and a pressure curve compatible with a vortex after visualization of each individual event. **(c)** Selection of events in (b) that also have a simultaneous drop in the light measured by the RDS Top7 photodiode with a drop of at least 0.5%. Histograms have been corrected from sampling effects. The error bars represent the standard deviation obtained in Monte Carlo simulations that reproduce the number of events detected per hour, using a fixed probability equal to the total number of events divided by the total number of hours of observations. The

central value represents the mean number of events detected per hour. **(d-h)** Examples of a variety of pressure drops including: **(d)** weak vortices typical of the early morning; **(e)** night-time pressure drops coincident with increases in temperature and driven by thermal pulses from the RTG when the wind flows from the back of the rover to the Remote Sensing Mast (wind data not shown); **(f)** the most dusty event captured in the first 250 sols, also one of the most intense and longest; **(g)** long and noisy pressure drops typically found at noon and suggestive of the passage of the boundaries of convective cells; **(h)** long vortex just after sunset. Further information on events like (f) and (g) is given in²³.



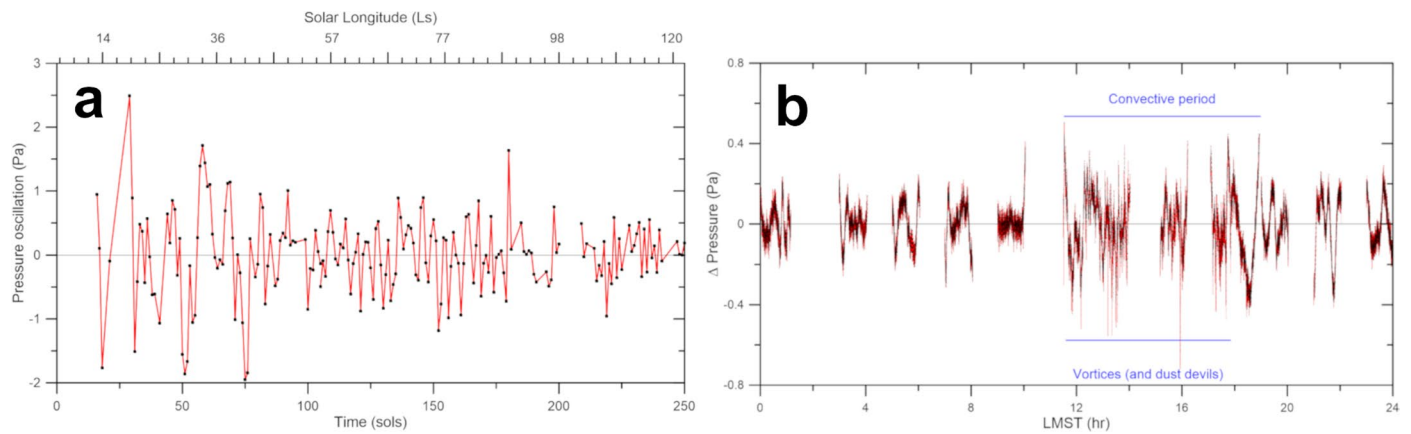
Extended Data Fig. 7 | Example of a Dust Devil record observed by MEDA, on sol 166. Dust Devil record observed on sol 166; the pink line reflects the sudden pressure drop caused by the passage of the convective vortex, while the blue line

shows the jump caused in the radiation ratio measured by TIRS and RDS, versus the same magnitude on preceding sols (cyan line). The data shown in the plot are the result of the mean over 10-sec intervals, plus-minus the standard deviation.



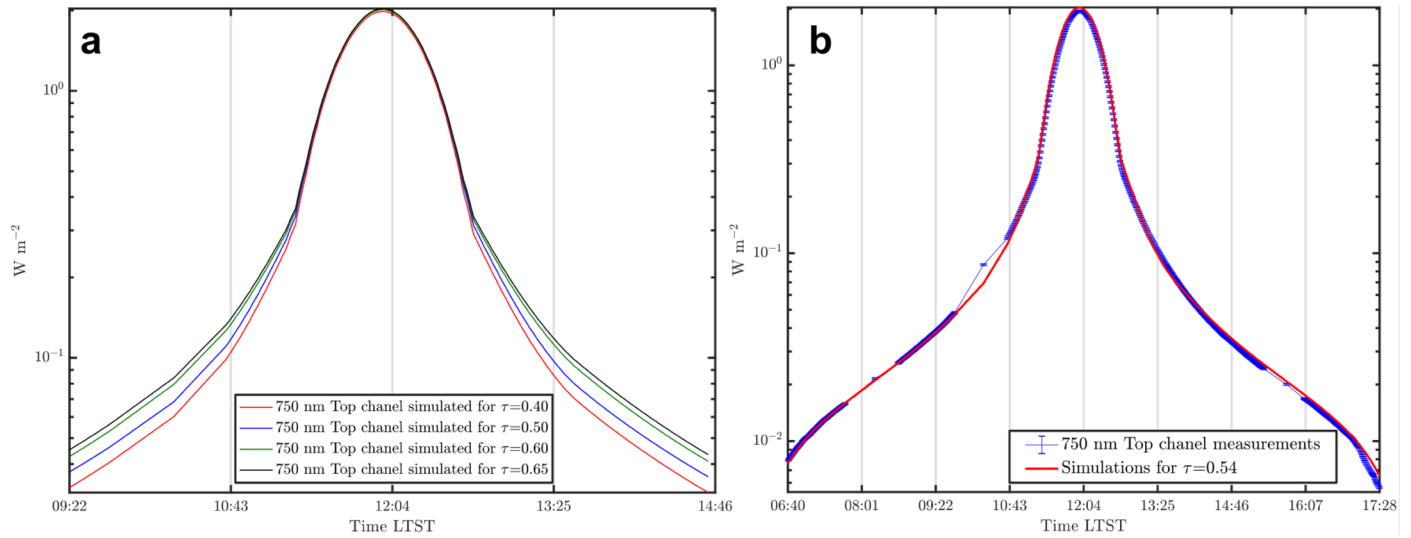
Extended Data Fig. 8 | Evolution of VMR and RH on sols of maximum variability. MEDA instrument has recorded a more complex hydrological cycle than expected. **(a)** Detail of the daily evolution of RH in characteristic sols (sols 104 to 110), where the complex and temporally variable structure of the

nocturnal hydrological cycle can be observed, sometimes not foreseen by the simulation models. **(b)** Daily evolution of the VMR for the sols shown in (a). A large increase in the VMR was observed on the evening of sol104.



Extended Data Fig. 9 | Analysis of pressure deviations recorded by MEDA. Deviations from the recorded pressure values suggest the possibility of high-frequency traveling waves. **(a)** Oscillations obtained in the differences between the daily mean values in Fig. 6a and the polynomial fit of degree 5 of

those values (coefficient of determination, R-squared = 0.985), where 2 intervals are observed: before and after sol -80. **(b)** Oscillations obtained in the infra-daily differences. Due to their properties, these oscillations are compatible with the propagation of gravity waves.



Extended Data Fig. 10 | Estimation of the optical properties of atmospheric dust from RDS data. Simulated signals for RDS Top5 channel for different opacities, and effective radius. **(a)** RDS Top5 channel signals simulated for different dust opacities and, a constant dust effective radius of $r_{eff} = 1.2 \mu m$. **(b)** Best fit between the simulations and the observations obtained.